

Amelia: A Large Model and Dataset for Airport Surface Movement Forecasting

Ingrid Navarro*, Pablo Ortega-Kral*, Jay Patrikar*[†], Haichuan Wang, Zelin Ye, Jong Hoon Park,
Jean Oh[‡] and Sebastian Scherer[‡]
The Robotics Institute, Carnegie Mellon University, Pittsburgh PA, USA

The growing demand for air travel requires technological advancements in air traffic management as well as mechanisms for monitoring and ensuring safe and efficient operations. In terminal airspaces, predictive models of future movements and traffic flows can help with proactive planning and efficient coordination; however, varying airport topologies, and interactions with other agents, among other factors, make accurate predictions challenging. Data-driven predictive models have shown promise for handling numerous variables to enable various downstream tasks, including collision risk assessment, taxi-out time prediction, departure metering, and emission estimations. While data-driven methods have shown improvements in these tasks, prior works lack large-scale curated surface movement datasets within the public domain and the development of generalizable trajectory forecasting models. In response to this, we propose two contributions: (1) *Amelia-48* dataset, a large surface movement dataset collected using the System Wide Information Management (SWIM) Surface Movement Event Service (SMES). With data collection beginning in December 2022, the *Phase I Amelia-48* dataset provides more than a year’s worth of SMES data (~30TB) and covers 48 airports within the US National Airspace System. In addition to releasing this data in the public domain, we also provide post-processing scripts and associated airport maps to enable research in the forecasting domain and beyond. (2) *Amelia-TF* model, a transformer-based next-token-prediction large multi-agent multi-airport trajectory forecasting model trained on 292 days or 9.4 billion tokens of position data encompassing 10 different airports with varying topology. The open-sourced *Amelia-TF* model is validated on unseen airports with experiments showcasing the different prediction horizon lengths, ego-agent selection strategies, and training recipes to demonstrate the generalization capabilities.

[[Website](#) | [Dataset](#) | [Model](#) | [Code](#)]

I. Introduction

Within the US National Airspace System (NAS), the first two months of 2023 saw more aircraft close-calls than they had during all of the previous five years combined [1]. While this disturbing trend can be attributed in part to deficiencies within the Air Traffic Control (ATC) facilities [2], the projected future NAS demands entail an increase in airspace capacity [3], further straining the existing infrastructure. The year of 2023 also broke the record for the most number of travelers processed by TSA by screening 2.9 million passengers in a single day [4, 5].

An increase in air traffic leads to congestion on airport surfaces, adversely affecting customer experience, increasing fuel consumption [6], and greenhouse emissions [7]. As such, this growing demand for air travel along with the planned introduction of Advanced Aerial Mobility (AAM) concepts like eVTOLs require technological advancements in air traffic management [8], including mechanisms for monitoring and ensuring **safe** and **efficient** operations.

Data-driven motion prediction models for airport surface operations could help **prevent unsafe situations** such as near-misses. These models, for instance, could be used for forecasting aircraft future states and proactively calculating collision risks [9, 10], or for preemptively identifying behavior that could lead to high-risk situations [11, 12]. Currently, the *Airport Surface Detection Equipment – Model X* (ASDE-X) system already provides straight-line predictions [13] including predictions for when a pilot lines up to land on a taxiway. Data-driven models could improve these predictions by accounting for multi-modal information, such as other aircraft, different airport geometries and semantics,

*Equal Contribution

[†]Corresponding Author

[‡]Equal Advising

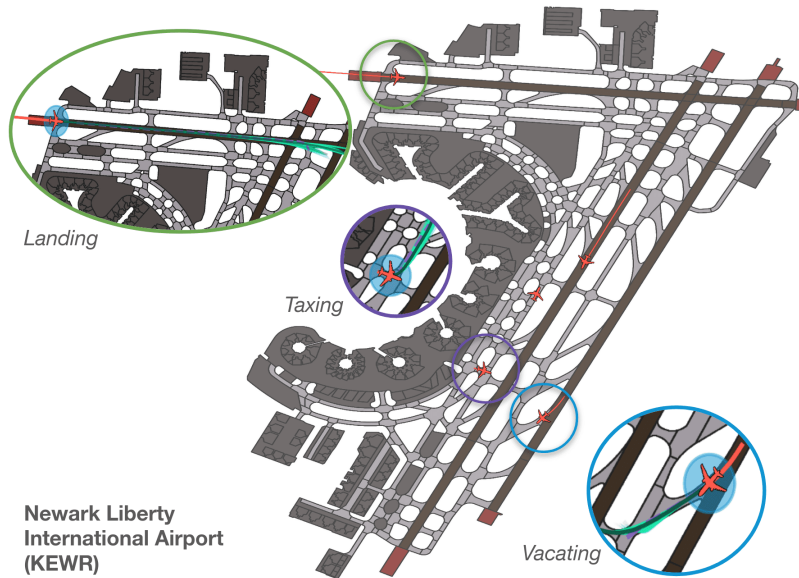


Fig. 1 An example of a scene collected from the *Newark Liberty International Airport (KEWR)* in which different aircraft within the scene are performing various maneuvers, e.g., landing (top-left), taxiing (bottom-left), and vacating (bottom-right). The figure also shows zoomed-in *Amelia-TF*'s predicted trajectories (green segment) for each agent, given their historical information (red-orange segment) and context (map) information.

weather information, and aircraft dynamics [14, 15]. These models can also be directly employed by fully autonomous and remotely-operated AAM aircraft enabling informed situational awareness using onboard sensors for intelligent navigation [16, 17] and automated go-around decisions.

In addition to collision assessments, predictive models could improve **airport management efficiency** [18]. For instance, by estimating taxi-out times, predictive models could also be used for departure metering to coordinate pushbacks from the gate [19, 20]. Other operational aspects like deicing schedules [21] and time-of-arrival estimates [22] could also be explored. While prior works have addressed some of these challenges in part, the lack of unified architectures and open-sourced resources has hindered the **generalizability and scalability** of these methods.

This work, therefore, aims to collect and open-source a **large-scale dataset** of airport surface operations, as well as a **large model** for motion forecasting in said space. To do so, we take inspiration from the natural language processing and computer vision communities which, in recent years, have developed large-scale modeling techniques that have achieved remarkable performance in language- and vision-based tasks. At their core, these models are based on sequence-to-sequence transformer [23] architectures, which leverage large datasets in a self-supervised fashion to predict masked token information enabling them to learn relationships between long sequences of data points. Motivated by these methods, we collect a large-scale dataset of airport surface operations and use it to train a large trajectory forecasting model to predict aircraft trajectories across multiple airports. By training on a pre-selected subset of airports and evaluating our model on unseen airports, we demonstrate the generalization capabilities of the trained model on unseen airport geometries and agent-to-agent interactions. Generalization across airports is relevant as it allows the model to be deployed in airports with scarce or no prior databases while also improving predictions on airports within the database by transferring implicit notions of coordination from one airport topology to another. Thus, even if a particular interaction might not have occurred at a particular airport, the ability of large models to reason about interactions in novel settings should enable them to predict coherent patterns of interaction for any airport under consideration.

To summarize, this work provides **two distinct contributions**. The first is the introduction and open-sourcing of a large-scale dataset, dubbed *Amelia-48*. The dataset is collected using the Federal Aviation Administration's (FAA) System Wide Information Management (SWIM) Program and represents data from 48 airports and Terminal Radar Approach Control (TRACON) facilities collected starting Dec 1st of 2022. In addition to the SWIM data, we also collect and release airport surface maps derived from the OpenStreetMap (OSM) database. These maps are collected, cleaned, and released in the form of easy-to-use lightweight undirected graphs with semantic markings for important

attributes such as taxiways, runways, hold-short lines, etc. We provide open access to raw as well as processed data to motivate further research not only in surface movement forecasting but also in allied fields like anomaly detection and transportation research. The second contribution of this work is detailing and open-sourcing *Amelia-TF*, a large trajectory forecasting model trained on this dataset. *Amelia-TF* is a transformer-based model that predicts possible future motions of individual aircraft conditioned on the aircraft’s history, agent-to-agent interactions, and airport geometry. We evaluate *Amelia-TF* on several unseen airports using standard metrics for trajectory prediction. Detailed ablations on various design choices are provided for comparative analysis.

The rest of the paper is organized as follows: Section II provides a brief overview of existing datasets and models within the trajectory forecasting field, both within the domain of aviation as well as other domains. Then, in Section III, we describe our *Amelia-48*’s collection and processing methodology in Section III and provide data validation and statistical analyses therein. We, then, introduce *Amelia-TF*’s architecture and design details in Section IV. We outline our experimental setup to assess our model’s performance in Section V, and provide corresponding results and discussion in Section VI and VII. Finally, we provide more in-depth details for our architecture and complementary results in the Appendix.

Note to the reader: This paper is best read and analyzed in color.

II. Related Work

A. Trajectory Forecasting Datasets

Research in recent years has prominently featured data-driven approaches to understanding and predicting human motion in crowded, dynamic spaces. The majority of the research within this field has centered around studying pedestrian behavior, where datasets such as UCY [24], ETH [25], Stanford Drone Dataset [26], among others [27] have commonly been used for benchmarking motion prediction methods. These datasets generally feature settings such as college campuses and city streets. In a similar vein, the domain of urban driving has also been heavily researched within the field, in which datasets like Waymo Open Motion Dataset [28], Argoverse [29], and nuScenes [30], which focus on urban settings and highways. These datasets generally leverage complex sensor suites which enable them to capture rich, multi-modal information, including detailed maps, semantic annotations, and different agent types (e.g., pedestrians, vehicles, and cyclists), as opposed to pedestrian datasets, which are generally of smaller scale and unimodal, comprising only per-agent trajectory information in the form of 2D coordinates.

In contrast, the domain of aviation has not been studied as extensively as the domains described above. Previous works [31] have criticized the dominance of proprietary, non-public data in aviation research, finding that 68% of the works reviewed utilized solely proprietary data. In response, *TrajAir* [32], along with its follow-up work *TartanAviation*[33], for instance, was recently introduced as a multi-modal dataset in the public domain for motion prediction in general aviation. Comprising weather data and 3D trajectory data, *TrajAir* aimed to learn how pilots interact in non-towered airports, but focused only on one airport. Accordingly, in response to the lack of curated large-scale publicly accessible datasets in this domain, we release the *Amelia-48* dataset. To the best of our knowledge, *Amelia-48* is the largest dataset of its kind and is geared towards use by researchers even beyond those interested in airport motion forecasting.

B. Scene Representation for Trajectory Forecasting

Within the field of motion prediction, different modalities can be utilized to represent agents’ states and the contextual information that makes up a scene. An agent’s trajectory, for instance, can be characterized as positional information, and/or other components such as heading and acceleration information. These data can be generally expressed in a global [32], agent-centric [34], ego-centric [35], or viewpoint-invariant [36] frame. We follow an ego-centric representation, encoding a scene relative to a single agent, *a.k.a.* the ego-agent. While ego-centric representations may suffer from higher sample complexity [36], they are a more intuitive scene representation than agent-centric ones which encode each agent’s feature independently, ignoring direct agent-to-agent relationships. Moreover, this representation is easier to scale and generalize than global representations. While viewpoint invariant methods aim to tackle the aforementioned limitations through shared encodings that don’t depend on a reference frame, they are beyond the scope of this work.

Context awareness is essential for motion forecasting as it enables modeling how a scene’s environment conditions an agent’s motion. The most common context modality is map information. Maps can be used as rasterized images [37] generally representing a top-down view of the scene using simple geometries where semantic information is often preserved through color or one-hot encodings. Rasterized maps have two common disadvantages. First, the implicit

nature of the encoding makes it unsuitable for complex scenarios that require capturing fine-grained nuances such as direction and connectivity. Second, they can be computationally expensive as finer details might require significantly higher-quality images to avoid information loss [38, 39]. Various works have proposed cheaper representations that require encoding maps as graphs. For instance, [39] proposed a vectorized encoding of the maps expressed as groups of 2D cartesian segments whose relationship is captured through directional edges. This representation has been widely adopted [35, 40] as it produces less computationally intensive and more structured representation. Similarly, to imbue structure more explicitly and avoid information loss, [38] represents map information as road graphs where relationships between map elements are encoded via adjacency matrices. Following the recent success of structured map characterization [38, 39], we design vectorized graphs to represent map information where semantic information is included via one-hot encodings and node relationships as adjacency matrices. Finally, while other modalities such as weather information [32], and natural language [41] have also been explored within the field of motion prediction, they're out of the scope of this work.

C. Trajectory Forecasting Models

Data-driven trajectory prediction models are generally built upon two main components: a *scene encoding* and a *future prediction*. **Scene encoding** aims at learning rich features from the scene, modeling temporal, agent-to-agent, and agent-to-map relationships. Typically, dedicated encoders are utilized to extract unimodal representations [32, 34, 39] which are then fused at a later stage. Other approaches can be used to learn cross-modal or hierarchical representations [42], which allow for a more direct feature *interaction* modeling between the modalities. To capture temporal relationships upon these features, commonly used methods include Recurrent Neural Networks (RNNs) [34, 43], Temporal CNNs (TCNs) [32, 44], Transformers [35, 40, 45]. While both RNNs and TCNs have been shown to perform comparably RNNs are often deemed more computationally expensive and unstable to train [34, 44], but remain widely used [32, 34, 36]. Transformer-based approaches have surged in popularity within the trajectory prediction, showing improved computational efficiency and producing richer representations [35]. To model agent interactions pooling- and attention-based methods are typically used. Pooling [43] focuses on downsampling information via average or maximum operations over hidden states but often lacks interpretability. Attention-based methods [32, 34, 45], in contrast, focus on learning relevant and more interpretable agent-to-agent [32, 34], as well as agent-to-context [35, 42] relationships.

The motion prediction community generally deems the future as multimodal, i.e., for a given history, multiple future actions can be executed. **Future prediction**, thus, involves representing this inherent characteristic by producing a distribution of futures for a given scene. The community has generally drawn upon probabilistic models, where two prominent methods are Conditional Variational Autoencoders (C-VAE) as in [32, 34, 36] and Gaussian Mixture Models (GMM) [35, 40, 46]. CVAEs are generative methods that learn a conditional mapping between the input data and a latent space representation, but can struggle with mode collapse and are often deemed less interpretable. GMMs, in contrast, often provide a more compact and interpretable representation coupled with confidence scores.

Inspired by recent state-of-the-art methods [35, 40] our model, *Amelia-TF*, is built as follows: we encode scene information following a hierarchical method for feature representation [42] using a transformer-based backbone as in [35]. And, we adopt an MLP-based GMM prediction header as [40, 46] to perform future forecasting.

Finally, within the aviation domain, closest to our work is [14], which also proposes prediction models characterizing airport surface movement operations. In this work, the authors leverage the FAA's SWIM information system to analyze four hours' worth of movement at two airports, identifying the 2D position of each agent and state described in terms of acceleration and velocity as attributes of interest. Another work [47] uses one-week ADS-B data collected at Singapore Changi Airport. While these works do not release the data in the public domain, a significant drawback is the lack of generalizability to other airports due to a limited scope and scale.

III. Amelia-48 Dataset

Surface area operations refer to aircraft and vehicle movements on or near the airport surface. In this work, we restrict the surface movement definition to include aircraft landing, taking off, or taxiing within the marked airport movement area along with vehicles. We are interested in predicting agent behavior within this area and therefore, we aim to capture any aircraft and vehicle trajectory that enters it. The scope ends when the agent either exits the area or crosses the non-movement boundary markings on the airport surface. To use the collected data for training a trajectory forecasting model, we transform the raw position reports into smooth trajectories that include agent metadata. We ensure that the processed data format is compatible with existing dataloaders for machine learning (ML) libraries. The released dataset has three main components: raw data with position reports, processed data with interpolated trajectories, and

map information. The details of our data collection, processing, and validation methodologies are described in the following subsections. Specifically, in Section III.A we detail our collection methodology for the raw position reports. Then, Section III.B describes our trajectory pre-processing pipeline, and Section III.C our map collection and processing pipeline. Finally, in Section III.D, we provide a data validation analysis for a set of 10 airports, selected to validate our proposed model (See Section IV) and experimental setup (See Section V).

A. Raw Data Collection

The System Wide Information Management (SWIM) Program is a NAS-wide information system that supports Next Generation Air Transportation System (NextGen) goals [48] by serving as a repository of a multitude of aviation data. For this work, we particularly use the SWIM Terminal Data Distribution System (STDDS), which aggregates terminal data from various sources like Airport Surface Detection Equipment – Model X (ADSE-X), and Airport Surface Surveillance Capability (ASSC) into easily accessible information. This information is streamed via the NAS Enterprise Messaging Service (NEMS) as a subscription. Within the STDDS, the Surface Movement Event Service (SMES) provides position reports for aircraft and vehicles operating within a few miles of the airport, covering approaching and ground movement events.

The raw dataset is a collection of SMES messages covering Terminal Radar Approach Control Facilities (TRACONs) within the NAS. The data collection started on Dec 1st, 2022, and represents around 30TB of raw trajectory data. The NEMS streams are recorded and stored on our in-house server. The recording scripts use two sets of 4 concurrent Advanced Message Queuing Protocol [49] connections for redundancy. Each connection records data for one hour and then closes the connection to offload the data to storage as a tarball. The format of the files follows the structure: ALL_<#connection>_<UnixTimeStamp>.tr.gz. Every hour, the first set starts recording on the hour, and the next one starts 30 minutes later. Thus, at any given point, 8 connections are active. Each connection deals with a manageable chunk of data to reduce onboard RAM usage and guard against data corruption. The scripts launch afresh automatically every 30 minutes, providing redundancy against server downtime and networking snags. The planned *Phase 1* data collection ended on Dec 1st, 2023, with planned *Phase 2* ending on Dec 1st, 2024.

B. Trajectory Data Pre-Processing

To process the raw XML SMES position report messages from NEMS, we further develop data pre-processing scripts following our previous work, *TrajAir* [32]. In this work, we choose to focus on 48 airports in the US. The preprocessing scripts produce clean interpolated data in formats accepted by most modern ML-based trajectory forecasting dataloaders. The process starts by defining a 3D geographical polygon fence around the airport and filtering the position reports that fall inside this fence following the constraints described earlier. Figure 2 shows two examples for the fences defined for two airports: *Ted Stevens Anchorage International Airport* (PANC) and *Los Angeles International Airport* (KLAX).

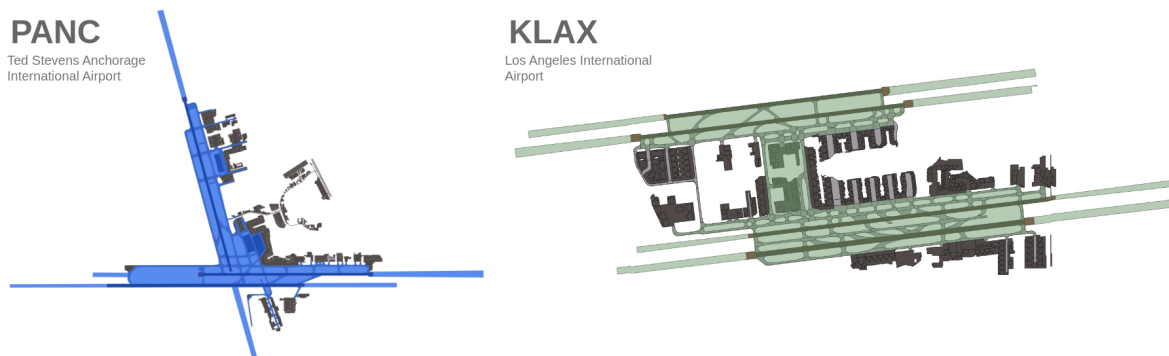


Fig. 2 Examples of polygonal fences used for collecting position reports within the airports' movement areas.

We further filter the position reports by capping the reported altitude above ground level at 2000 ft AGL. Apart from the location, we extract relevant metadata from each position report. The data is interpolated for each agent and resampled at 1Hz, providing additional rolling mean smoothing. We produce CSV files corresponding to one hour of data for each airport. Table 1 shows the various fields within each CSV with their units and descriptions. To get the local cartesian coordinates, we pick an arbitrary origin within the airport surface.

Table 1 List of fields with corresponding units and descriptions in the pre-processed *Amelia-48* dataset.

Field	Units	Description	Field	Units	Description
Frame	#	Timestamp	Altitude	feet	Agent Altitude (Mean Sea Level)
ID	#	STDDS Agent ID	Range	km	Distance from airport datum
Speed	knots	Agent Speed	Bearing	rads	Bearing Angle w.r.t. North
Heading	degrees	Agent Heading	Type	int	Agent Type [0:A/C, 1:Veh, 2:UNK]
Lat	decimal degs	Latitude of the agent	x	km	Local X Cartesian Position
Lon	decimal degs	Longitude of the agent	y	km	Local Y Cartesian Position
Interp	boolean	Interpolated data point flag			

C. Map Data Collection and Pre-Processing

We use OpenStreetMap (OSM) [50] and OSMNx [51] to collect and produce surface maps for each of the airports in *Amelia-48*. Raw OSM airport maps are routing graphs containing centerline information of the movement areas, pavement boundaries, and semantic information, e.g., taxiways, runways, hold-short lines, exit lines, aprons, etc. As an example, Figure 3.a) shows a small region of the Seattle-Tacoma Airport (KSEA) in its raw representation. Node elements within the graph contain geographical coordinates, i.e., (latitude, longitude), and local Cartesian coordinates, (x, y) , expressed w.r.t. an arbitrary origin coordinate unique to each airport. The connection between nodes is represented as polyline or polygon elements characterizing linear regions within the map, which combined, make up the airport’s surface area. Although this map representation is semantically rich and detailed, we seek to obtain a more compact and computationally efficient map that only maintains elements of interest. Here, our main interest is to keep centerline information and semantics of the map’s movement areas of runways and taxiways. We, therefore, apply a series of automated steps to the raw maps to obtain an easy-to-use and compact representation which we describe next. We begin by filtering out all edges and nodes that comprise the boundaries of pavement areas. We only maintain the semantic information of the following classes: runways, taxiways, and hold short lines, i.e., markings that indicate the exit boundary of runway protected areas. An example of a resulting graph after this step is shown in Figure 3.b).

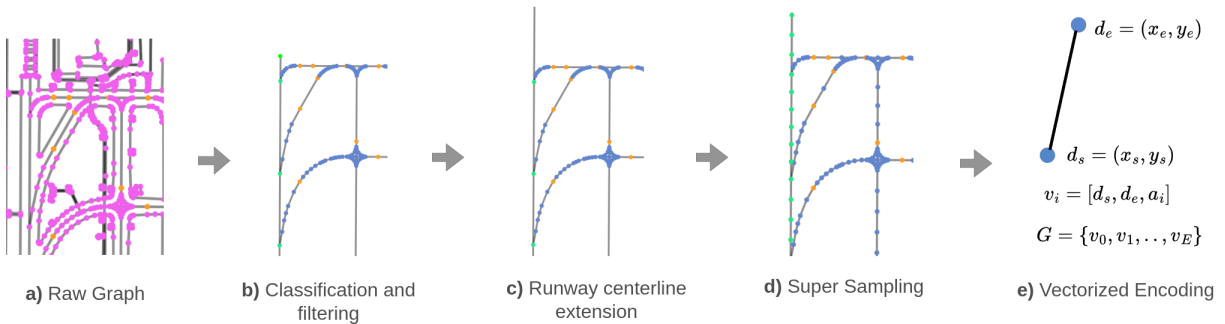


Fig. 3 Overview of the proposed map processing pipeline. a) Shows an example of the graphs obtained from OpenStreetMap in raw format. b) Nodes corresponding to pavement and marking areas are filtered out, keeping only our categories of interest **runway**, **taxiway**, or **hold-short line**. c) Runways are extended to obtain finer associations to a context region for landing and take-off rolls. d) Long edges are supersampled to refine graph’s granularity. e) The map is encoded as a graph with edges describing the nodes’ connections as vectors and semantic categories.

Since we are interested in capturing behaviors encompassing landing and take-off procedures, we extend the endpoints of each runway beyond the airport perimeter as shown in Figure 3.c). To ensure this extension follows along the runway centerline, we first calculate the runway bearing; for each end, we then calculate a point 1 nautical mile away along the bearing. While this step defines the final extents of the extended runway centerlines, this results in long edges that provide inaccurate positional matching for an agents’s position w.r.t. the map. Thus, as a final step, we apply node supersampling to the runway centerline extensions to obtain a finer graph. The resulting extended runway centerlines are shown in Figure 3.d).

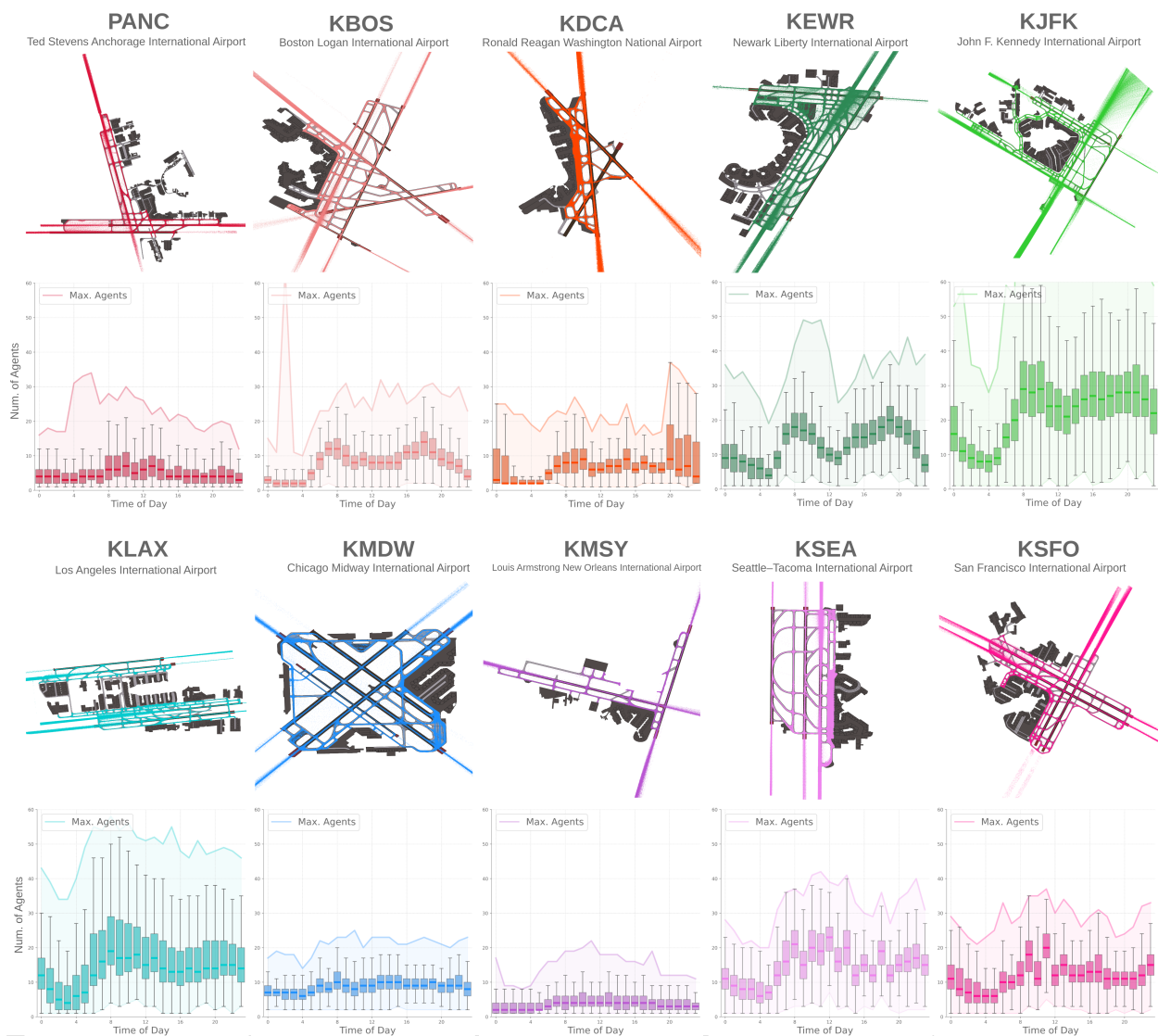


Fig. 4 Overview of the processed airport trajectory data. We study 10 airports with varying crowdedness and map topologies. For each airport, we overlay a month’s worth of processed trajectories spanning beyond runway limits to capture landing and take-off rolls. We also show each airport’s crowdedness per hour-of-day.

Upon these steps, we follow [39] to encode the graph in a vectorized manner depicted in Figure 3.e). Here, we describe each edge in the navigation graph as a vector, $v_i = [d_i^s, d_i^e, a_i]$, where $d_i^s \in \mathbb{R}^{1 \times 4}$ and $d_i^e \in \mathbb{R}^{1 \times 4}$ are the edge’s start and end nodes containing the geographical and relative coordinates. Then, $a_i \in \mathbb{N}^{1 \times 3}$ represents any semantic attributes of the edge; in our work, this is a one-hot encoded categorical value indicating one of the three semantic classes of interest **runway**, **taxiway**, or **hold-short line**. Finally, we express the graph $\mathcal{G}(V, E)$ as $\mathcal{G} = \{v_1, v_2, \dots, v_E\}$.

D. Dataset Analysis

We now provide a thorough analysis of the trajectory and map data described in the previous sections. For ease of analysis, we select 10 airports on which to run our analyses. To favor diversity in the data, we select airports with varying traffic levels and map topologies and provide supporting evidence of our selection criteria in the subsequent sections. Our selected airports are shown in Figure 4 along with their corresponding names and International Civil Aviation Organization (ICAO) identifier. For brevity, throughout the paper we use an airport’s ICAO identifier to refer to it.

1. Trajectory Data Analysis

We process 292 days worth of data, a month approximately 30 days for each selected airport. Table 2 summarizes each airport’s traffic information. We include the months from which we sampled the data, the *total* and *per-category* number of unique agents, unique data points, and percentage of said data points that were interpolated (See Table 1, Interp).

Table 2 Raw trajectory data summary per airport showing the *total* and *per-category* number of unique agents and data points along with the percentage of interpolated points. For readability, numbers are reported with two significant digits. M is used to abbreviate millions and K for thousands.

Airport	Month	Total		Aircraft		Vehicles		Unkown	
		Num. Agents	Num. Data Points (% Interpolated)	Num. Agents (% w.r.t. Total Agents)	Num. Data Points (% Interpolated)	Num. Agents (% w.r.t. Total Agents)	Num. Data Points (% Interpolated)	Num. Agents (% w.r.t. Total Agents)	Num. Data Points (% Interpolated)
PANC	Nov	131.35K	15.43M (0.22%)	16.96K (12.91%)	5.88M (0.15%)	4.01K (3.12%)	2.51M (0.84%)	110.29K (83.97%)	7.035M (0.06%)
KBOS	Jan	94.99K	23.39M (0.62%)	33.44K (35.20%)	14.77M (0.45%)	4.27K (4.50%)	2.94M (1.33%)	57.29K (60.30%)	5.68M (0.68%)
KEWR	Mar	140.81K	30.86M (4.86%)	38.86K (27.59%)	20.81M (5.67%)	2.21K (1.57%)	1.23M (8.32%)	99.75K (70.84%)	8.81M (2.47%)
KDCA	Dec	61.85K	17.78M (9.94%)	25.81K (41.73%)	8.22M (8.29%)	1.30K (2.10%)	1.00M (16.82%)	34.74K (56.17%)	8.56M (10.72%)
KJFK	Apr	645.41K	52.82M (9.89%)	45.15K (6.99%)	28.023M (12.03%)	156 (0.02%)	66.31K (4.66%)	600.11K (92.98%)	24.73M (7.47%)
KLAX	May	451.80K	42.81M (0.49%)	60.24K (13.33%)	24.67M (0.30%)	14.92K (3.30%)	2.79M (3.33%)	376.70K (83.38%)	15.35M (0.27%)
KMDW	Jun	211.92K	28.51M (0.84%)	22.47K (10.61%)	6.69M (0.32%)	6.28K (2.97%)	6.15M (3.35%)	183.22K (86.46%)	15.67M (0.07%)
KMSY	Jul	49.35K	10.37M (0.13%)	10.42K (21.12%)	2.57M (0.08%)	54 (0.11%)	39.89K (3.07%)	38.87K (78.77%)	7.75M (0.13%)
KSEA	Aug	378.54K	38.48M (0.23%)	50.08K (13.23%)	26.13M (0.19%)	290 (0.08%)	274.94K (1.02%)	328.17K (86.70%)	12.077M (0.31%)
KSFO	Sep	185.87K	36.013M (2.91%)	37.36K (20.10%)	16.67M (2.84%)	14.57K (7.84%)	5.65M (3.26%)	133.94K (72.06%)	13.69M (2.87%)
Total		2,351,883	296,448,313 (3.46%)	340,791 (14.49%)	154,436,226 (3.84%)	48,149 (2.05%)	22,653,655 (3.63%)	1,963,086 (83.47%)	119,354,023 (2.95%)

From this table, we observe a wide variety of traffic levels across airports, with KMSY and KJFK being the least and most crowded ones, respectively. Across all airports, we processed ~2.35M unique agents spanning ~300M unique global data points. Here, only 3.46% of the data points were interpolated, ranging between 0.13% and 9.94% for each airport. The table also shows that the majority of the collected data corresponds to unidentified agents, i.e., agents that were classified neither as *aircraft*, nor *vehicle*, representing 83.47% of the unique agents. We note, however, that we have no explicit control of the agent categorization process and improvements to the category identification are out of the scope of our work.

Figure 4 shows the processed trajectories overlaid on top of its corresponding map. Note that, throughout the paper, we follow the same airport color-coding as in the figure for consistency. The trajectories span beyond the runway limits to allow capturing landing and take-off rolls. In addition to the trajectory information, the figure depicts each airport’s crowdedness by hour of day. We show a boxplot summarizing the *per-hour* (*x*-axis) *agent density* (*y*-axis) across the ~30 days. Finally, the thick line plot shows the maximum recorded agent density. From these plots, we can observe two main things. First, we can generally see density peaks in the morning and afternoon, indicating higher levels of activity. Second, the plots let us contrast traffic densities and variances within each airport. For instance PANC, KMDW and KMSY are significantly less crowded than KJFK and KLAX.

Finally, we analyze aircraft motion profiles across the collected airports in Figure 5. Specifically, we focus on (1) heading change in subsequent timesteps, and (2) mean speed and (3) mean acceleration per trajectory. We see that speed and heading have an ample spread, reflecting the different aircraft behaviors, e.g., take-off taxiing, vacating, etc. The acceleration histogram shows the majority of sequences fall within the 0 m/s^2 acceleration bin. This aligns with the behavior of stationary aircraft awaiting clearance or gate assignment. Noticeable high deceleration and acceleration profiles correspond to aircraft landing and taking off. While diverse across airports, the speed, acceleration, and heading change follow a similar trend. This indicates consistent aircraft behavior and verifies that Amelia-48 accurately captures the desired ground operation behaviors.

2. Map Data Analysis

We now show that our selected airports also vary at the topological level. Table 3 summarizes various aspects of each airport’s map. First, it shows that our selection includes airports with 2 to 5 runways in different configurations. We included airports with only *parallel* (P) and *interesecting* (I) runways, while also considering more complex topologies which include various combinations of *both* (B) types.

The table also provides a statistical summary for each airport’s graph. We show the *total* and *per-category* number of nodes in each graph. From these numbers, we can contrast the relative complexity between maps, e.g., a *low*-complexity map such as KMSY which only has ~1.5k nodes vs. a *high*-complexity one like KLAX with ~11k. We also complemented the summary with the *min.*, *max.*, *avg.* and *std. dev.* node-to-node distance values.

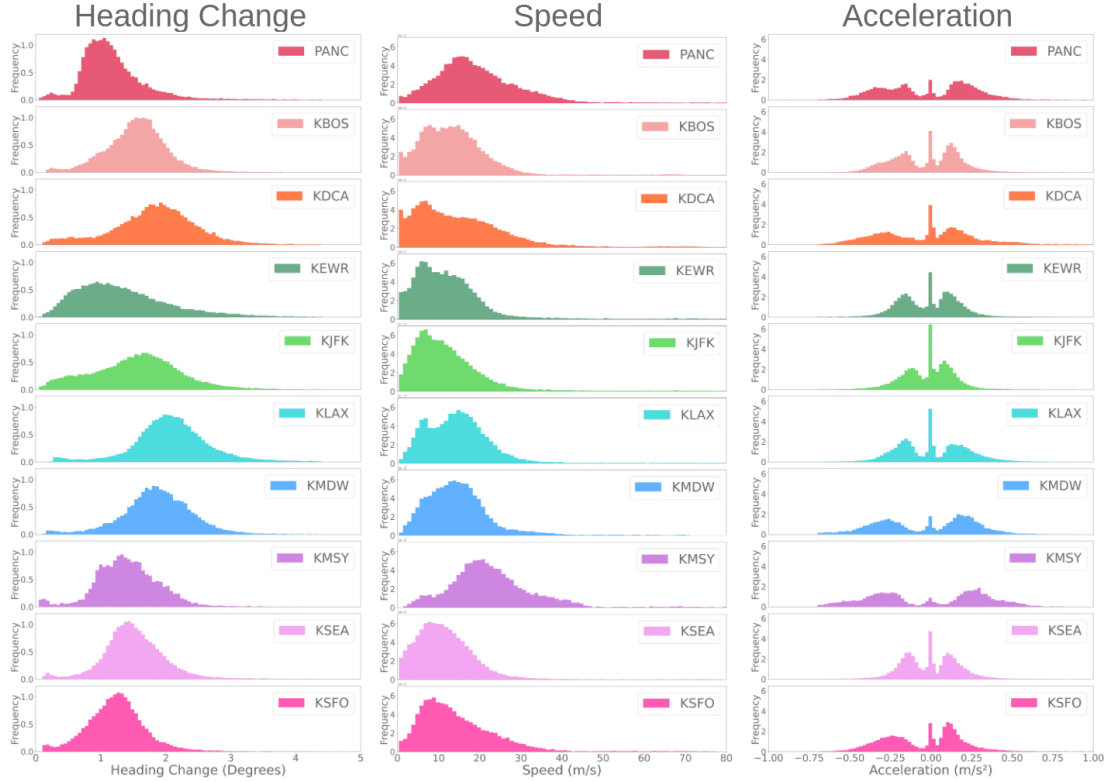


Fig. 5 Aircraft motion profiles per airport. The first column shows the mean heading change per timestep. The second and third columns show the mean speed and acceleration per trajectory. All plots are shown as probability densities.

Table 3 Map data summary per airport. We show runway count and topology, *total* and *per-category* node count, and node-to-node distance statistics.

Airport	Num.	Runway	Graph Nodes				Node-to-Node Distance			
	Runways	Topology	Total	Runway	Taxiways	Hold Line	Min	Max	Avg.	Std. Dev
PANC	3	B	8,016	676	7,134	206	0.19	79.94	21.24	23.91
KBOS	5	B	5,056	944	3,826	286	0.94	79.86	26.99	27.03
KDCA	3	I	8,154	438	7,590	126	0.26	79.92	7.87	18.72
KEWR	3	B	4,804	1,424	3,090	290	0.35	79.88	42.25	29.66
KJFK	4	B	7,090	762	5,820	508	0.20	79.97	29.15	26.33
KLAX	4	P	10,728	766	9,224	738	0.27	79.91	18.12	22.42
KMDW	5	B	4,132	582	3,122	428	1.18	79.96	22.28	24.63
KMSY	2	I	1,408	474	790	144	1.70	79.82	47.76	29.59
KSEA	3	P	4,782	540	4,000	242	1.24	79.99	22.39	25.50
KSFO	4	B	9,032	686	7,992	354	0.23	79.88	18.48	23.23

P: parallel runways, **I:** intersecting runways, **B:** both, parallel and intersecting runways.

IV. Amelia-TF Model

Amelia-TF is an end-to-end trajectory forecasting model that aims to characterize *relevant* surface area operations as those described in Section III. To achieve this, we build upon the intuitions from prominent state-of-the-art models to design a model capable of learning strong feature representations [35, 40], as well as automated methods for selecting

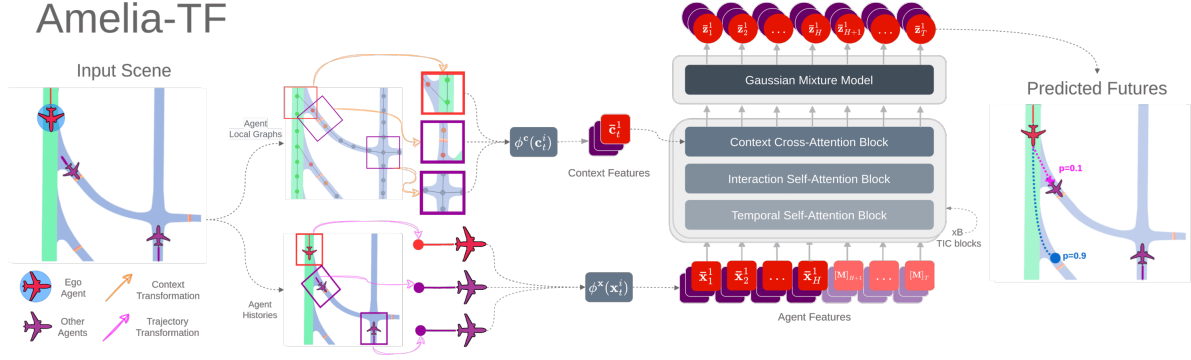


Fig. 6 Overview of Amelia-TF. For a given scene, Amelia-TF takes agent trajectories and their corresponding local context graphs as modalities of information and transforms them w.r.t. a pre-selected ego-agent. It then encodes the scene via blocks of transformer layers that attend over temporal and agent-to-agent, and agent-to-context relationships within a scene. Finally, the resulting feature is fed to a Gaussian Mixture Model which produces a distribution over the possible agent futures.

relevant scenes and agents to characterize [52]. Specifically, our model comprises three main submodules: (1) a **scene representation** module that determines the agents of interest in the scene and encodes per-agent features; (2) a transformer-based **scene encoder** [35, 42, 53], which hierarchically encodes the temporal, agent-to-agent and agent-to-context relationships within a scene, and; (3) a **trajectory decoder** that models the set of possible futures with associated confidence scores using a Gaussian Mixture Model.

We show an overview of Amelia-TF in Figure 6, and provide further details for each of its components in the subsections that follow. We begin by providing a mathematical formulation for the trajectory forecasting task in Section IV.A. We, then, detail scene representation methodology in IV.B, and model details in sections IV.C and IV.D, respectively. Finally, in Section IV.E, we describe the optimization objective used during training.

A. Problem Formulation

1. Notation Details

Following prior works [32, 34, 35], we define $\mathbf{x}_t^i \in \mathbb{R}^D$ as a D -dimensional vector that represents the state of an agent i at some timestep t . In this work, a state represents an agent’s 3D coordinates and heading, i.e., $\mathbf{x}_t^i = (x, y, z, \theta)_t^i$. Then, we represent a trajectory as a sequence of states from some timestep t_m to another timestep t_n as $\mathbf{x}_{t_m:t_n}^i$. To represent a feature and a prediction we use the bar, e.g., $\bar{\mathbf{x}}$, and hat, e.g., $\hat{\mathbf{x}}$, respectively. We use parentheses for the super-scripts to refer to a layer number, e.g., $\bar{\mathbf{x}}^{(l)}$, represents a state feature at layer l . Finally, for ease of notation, we omit superscripts to refer to joint representations, e.g., $\mathbf{x}_t = [\mathbf{x}_t^1, \dots, \mathbf{x}_t^N] \in \mathbb{R}^{N \times D}$, is the joint state for all agents in a scene.

Along with agent poses, we leverage semantic graph representations, as those delineated in Section III.C to further contextualize each agent’s state. We define this context as $\mathbf{c}_t^i \in \mathbb{R}^{P \times C}$, where P is the number of nodes making up the graph, and C is the dimensionality of a node. We follow the same notation details to represent the context of an agent, \mathbf{c}_t^i , a trajectory of contexts, $\mathbf{c}_{t_m:t_n}^i$, and a joint context, \mathbf{c}_t . In general, context can be shared among all agents in the scene, or local for each agent in the scene. As we will detail in Section IV.B, we use a local context representation for each agent, which we interchangeably refer to as local patches.

2. Problem Statement

We now formulate the trajectory forecasting problem as follows. First, in this work, a scene represents the joint sequences of a set of agents in the environment of interest, along with their corresponding context information. Therein, consider a scene consisting of K agents, each with an associated trajectory of length T . Here, agents whose trajectories are shorter than T (e.g., agents that exit the scene earlier, or enter it later) are padded with zeroes. Each trajectory is then split into an observation (or *history*) and a prediction (or *future*) segment. The observed portion is defined as $\mathbf{x}_{t_o-H:t_o}^i$, where t_o is the last observed timestep, and H is the length of the agent’s observed history. Similarly, to represent the future horizon we use $\mathbf{x}_{t_p:t_p+F}^i$, where t_p is the first future time step and F is the length of the future segment. Note that

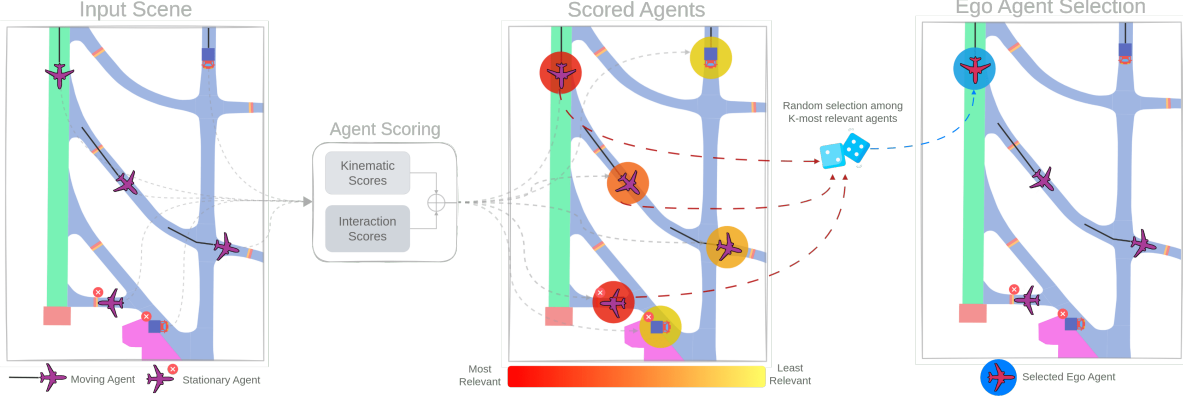


Fig. 7 Overview of our scene representation methodology. Given an input scene consisting of N agents, we compute a score for each agent representing its *kinematic* and *interactive* profile. To represent the final scene, we keep the K -most relevant, as deemed by the scoring function. Finally, the ego-agent is randomly selected among the K -agents.

$T = H + F$. Each trajectory has an associated context history, $\mathbf{c}_{t_o-H:t_o}^i$.

Then, for an agent i in the scene, the goal for a trajectory forecasting model is to learn a distribution of M possible future trajectories $\hat{\mathbf{x}}_{m, t_p:t_p+F}^i$, given the agents' observed histories and contextual information. Mathematically,

$$\hat{\mathbf{x}}_{m, t_p:t_p+F}^i \sim P_{\theta}(\cdot | \mathbf{x}_{t_o-H:t_o}, \mathbf{c}_{t_o-H:t_o}^i) \quad \forall m \in \{1, \dots, M\}$$

where θ represents the learned parameters of the model.

B. Scene Representation

In this work, we follow an ego-centric scene representation where we transform and encode all agents' trajectories and contexts within a scene w.r.t. to a pre-selected *ego-agent*.

As expressed in previous sections, we aim to characterize *relevant* behaviors and interactions within airport operations. Examples of such behaviors include—but are not limited to—aircraft preparing for take-off, stationary aircraft near hold-short lines, aircraft landing and taxiing out. Raw scenes, however, may contain non-critical agents, such as stationary agents in low-conflict regions. Consequently, learning a distribution over possible futures for such agents could make the prediction task trivial. Thus, to encourage *Amelia-TF* to focus on more complex behavior, we build an automated method inspired by our previous work, *SafeShift* [52], for both, selecting relevant ego-agents and producing diverse and complex scene representations.

An overview and toy example of our scene representation and ego-agent selection methodology is shown in Figure 7. The example depicts an airport scene with a variety of behaviors: an aircraft landing on a **runway**, two aircraft vacating a **taxiway**, an aircraft waiting near a **hold-short line**, and two vehicles. To select the most relevant agents, our method takes each agent's trajectory and map information and computes a score indicating how *critical* it is; where the higher the score, the more critical the agent is deemed. Our score, specifically, is the result of a function describing a proxy for the agent's *kinematic* and *interaction* states.

For the **kinematic**, state we encode the agent's speed, acceleration, and jerk profiles as in [52]. We further account for stationary and slow-moving agents near hold-short lines, which are regions where an aircraft should stop before entering a runway. These are especially important since they help ensure an aircraft's proper positioning. Thus, to characterize these situations, we incorporate a waiting interval measure weighted by the inverse of the distance to the hold line. Then, for the **interaction** state, we consider each agent pair and measure their loss of separation value as in [16], as well as a measure indicating the minimum time to conflict point between the agents' trajectories and conflict regions in the map as [52].

Once each agent in the initial scene is scored, we select the K -most critical agents to represent the final scene. Next, we randomly choose the ego-agent, e , among the selected agents and transform the scene w.r.t. its pose at the last

observed timestep, $\mathbf{x}_{t_o}^e$. The final transformed trajectories, $\mathbf{x}_{t_o-H:t_o} \in \mathbb{R}^{K \times H \times D}$, are encoded into features as follows,

$$\bar{\mathbf{x}}_{t_o-H:t_o} = \phi^{\mathbf{x}}(\mathbf{x}_{t_o-H:t_o}) + \text{PE}(\mathbf{x}_{t_o-H:t_o})$$

where $\phi^{\mathbf{x}}$ is an MLP-based feature extractor and PE is a positional embedding.

Similarly, we encode the transformed context graphs, $\mathbf{c}_{t_o-H:t_o} \in \mathbb{R}^{K \times H \times P \times C}$ as,

$$\bar{\mathbf{c}}_{t_o-H:t_o} = \phi^{\mathbf{c}}(\mathbf{c}_{t_o-H:t_o})$$

where $\phi^{\mathbf{c}}$ is a map feature extractor based upon *VectorNet* [39]. Note that our model encodes individual local patches for each agent in the scene, in contrast to prior works where a shared global context is used for all agents in the scene [35, 39, 40]. The intuition behind it is that, in aviation, relevant interactions are not necessarily local as would often be the case for settings such as autonomous driving or navigation in human crowds. For instance, while an autonomous vehicle might be more interested in potential interactions with vehicles at a nearby intersection or conflict region, an aircraft might be interested in the potential interaction with an agent at the other end of the runway. In our domain, however, encoding the global airport map information in the scene may make it difficult for the model to generalize to unseen settings. Thus, we opt for a local context encoding and assume that relative distances between agents and context regions are preserved in the ego-centric scene transformation.

C. Scene Encoder

Our trajectory forecasting model follows a transformer-based encoder architecture which uses a factorized attention scheme for efficient computations as in [35]. The model maintains a $K \times F \times D$ representation across all transformer layers while interleaving two types of self-attention layers: a *temporal* and an *interaction* one, as well as a *context* cross-attention layer as shown in Figure 6. For brevity, we refer to a block comprising these three layers subsequently as a TIC block.

The **temporal** layer is designed as a causal transformer layer [53]. This layer is used for learning the time-wise dependencies within the trajectories by attending only to past features across the time dimension using a mask operator, \mathbf{M} , that only *looks* at the previous states from a given timestep. Then, the **interaction** layer is designed to learn agent-to-agent relationships by attending over the features across the agent dimension. For both of these encoder blocks and with a slight abuse of notation, we can express a single self-attention layer, l , as,

$$\bar{\mathbf{x}}^{(l)} = \text{MHA}(\text{query} = \bar{\mathbf{x}}^{(l-1)}, \text{key} = \bar{\mathbf{x}}^{(l-1)}, \text{value} = \bar{\mathbf{x}}^{(l-1)}, \text{mask} = \mathbf{M})$$

where $\text{MHA}(\cdot)$ is a multi-head attention block [23] which receives the joint feature from the previous layer, $\bar{\mathbf{x}}^{(l-1)}$, as the query, key, and value parameters, and produces an output feature, $\bar{\mathbf{x}}^{(l)}$.

The **context** cross-attention layer is then used to exploit the relationships between agent and map features. Here, thus, the $\text{MHA}(\cdot)$ uses the agents' joint feature as the query input, while the keys and values are obtained from the embedded context,

$$\bar{\mathbf{x}}^{(l)} = \text{MHA}(\text{query} = \bar{\mathbf{x}}^{(l-1)}, \text{key} = \bar{\mathbf{c}}^{(l-1)}, \text{value} = \bar{\mathbf{c}}^{(l-1)}, \text{mask} = \mathbf{M})$$

Our model's scene encoder is composed of multiple TIC blocks, stacked sequentially to obtain a richer representation. For implementation and architectural details, we refer the reader to the Appendix. Finally, for more details on the intuitions and benefits of using factorized attention mechanisms, we refer the reader to [35, 54].

D. Trajectory Decoder

To model the distribution of possible futures for an encoded scene, we adopt a Gaussian Mixture Model (GMM) as [40, 46]. Here, a GMM-based representation can be formulated as a weighted sum over the mixture of modes,

$$p(\mathbf{x}) = \sum_{m=1}^M \rho_m \cdot \mathcal{N}_m(\mathbf{x} - \boldsymbol{\mu}_{\mathbf{x}}, \boldsymbol{\Sigma}_{\mathbf{x}})$$

where each mode, m , in the mixture is conditionally independent over timesteps, producing a distribution \mathcal{N}_m with mean $\boldsymbol{\mu}_x \in \mathbb{R}^D$ and covariance $\boldsymbol{\Sigma}_x \in \mathbb{R}^{D \times D}$ over the joint state \mathbf{x} . Furthermore, each mode has a tied weight, ρ_m , which represents its likelihood over time, where $\sum_{m=1}^M \rho_m = 1$. We model the GMM as an MLP that receives the output feature at the final layer, L , of the scene encoder,

$$\bar{\mathbf{z}}_{t_p+F:t_p} = \phi^{gmm}(\bar{\mathbf{x}}_{t_o-H:t_o}^{(L)})$$

where, for each agent i , outputs a feature, $\bar{\mathbf{z}}^i \in \mathbb{R}^{M \times F \times 7}$, consisting of the Gaussian’s mean, variance, and probability components for each mode over the predicted timesteps. The feature, thus, follows the format $(\mu_x, \mu_y, \mu_z, \sigma_x, \sigma_y, \sigma_z, \rho)_{m,t}$ for a given mode and timestep. Finally, the M predicted trajectories for a given agent can be obtained by simply extracting the means of the Gaussian components.

E. Training Objective

The final model is trained in an end-to-end manner using two training components; (1) a *regression* component, \mathcal{L}^{nll} , which back-propagates the average negative log-likelihood between the predicted trajectories and the ground truth, and (2) a *classification* component, \mathcal{L}^{ce} , representing the cross-entropy between the model’s predicted confidences for each of the M prediction heads and the one-hot encoded vector corresponding to the predicted future with smallest error. Our total loss is expressed as,

$$\mathcal{L}^{total} = \lambda^{nll} \mathcal{L}^{nll} + \lambda^{ce} \mathcal{L}^{ce}$$

where, $\lambda^{nll}, \lambda^{ce} \in \mathbb{R}$ are weighting hyperparameters.

V. Experimental Setup

Details of our experimental setup are described in this section as follows. In Section V.A we provide scene representation and model architectural and training details. Next, in Section V.B we cover the metrics used to assess the performance of Amelia-TF. Finally, in Section V.C we describe three proposed experiments to assess Amelia-TF. Additional implementation details are provided in the Appendix.

A. Implementation Details

- 1) **Dataset:** We consider the 10 airports introduced in Section III.D. We post-process 1 randomly chosen month of trajectory data, representing ~ 720 hours. As summarized in Table 2, each airport has between $\sim 11\text{M}$ and $\sim 42\text{M}$ unique global data points for a single month of data. To split the data into a *training/validation* and *testing* sets, we use a *day*-based splitting strategy where 80% of each airport’s collected days are used for training/validation and the remaining 20%, for testing. The days in each subset are chosen randomly.
- 2) **Scene Representation:** We split the data into scenes of $T = 60$ seconds to capture long-horizon interactions. We use a sliding window of $t = 1$ second to generate subsequent scenes. Within each scene, the first $H = 10$ seconds represent the observed (or history) segment and the remaining $F = 50$ seconds represent the prediction (or future) portion. In our experiments, however, we show results at $F = 20$ and $F = 50$ to assess our model’s performance over a *short* and a *long* horizon. We consider scenes containing a minimum of 2 agents and a maximum of 15. We then select a maximum of $K = 5$ agents as the *critical* agents following the selection process described in Section IV.B. For each of the selected agents, we obtain their local context consisting of the $P = 100$ closest points to their location at the last observed timestep, i.e., $t_o = H$. We keep the context fixed for the entire historical trajectory to reduce the computational expense of continually updating the context. Through this scheme, we obtain over **19.2M scenes**, comprising **$\sim 158.2\text{M}$ sequences** or **9.4B tokens**, where each token represents an agent’s state at a given timestep.
- 3) **Model Architecture:** We use a 2-layer MLP with layer normalization to extract agent features and a 4-layer MLP with batch normalization to extract context features. Our scene encoder is built using 3 TIC blocks. Each layer in the block consists of an MHA module with $h = 8$ attention heads and a 5-layer MLP that outputs the final feature embeddings. Finally, our GMM is built as a 2-layer MLP with a GELU activation and produces $M = 4$ output heads. The hidden dimensions of all MLPs are of size $D = 256$. The final model consists of **$\sim 89.8\text{M}$ parameters**. For full architectural details, please refer to Appendix.A.

- 4) **Training:** We train for at most 100 epochs with an early stopping strategy with a 10-epoch patience over the mADE metric. We use a standard Adam optimizer with a learning rate of $lr = 1e - 4$ and an on-plateau scheduler. For more implementation details, please refer to Appendix.B.

B. Metrics

We use commonly adopted metrics within the field of trajectory forecasting to assess the performance of *Amelia-TF*. The metrics descriptions and mathematical formulations are summarized below:

- 1) **Minimum Average Displacement Error (mADE):** considers the Euclidean error between the ground truth trajectory and the *best* predicted trajectory,

$$\text{mADE}(\hat{\mathbf{x}}, \mathbf{x}) = \frac{1}{FN} \sum_{i=1}^N \min_{m=1}^M \sum_{t=t_p}^F \|\hat{\mathbf{x}}_{m,t}^i - \mathbf{x}_{m,t}^i\|_2^2$$

- 2) **Minimum Final Displacement Error (mFDE):** similar to mADE, considers the Euclidean distance between the endpoints of the ground truth trajectory and the predicted one,

$$\text{mFDE}(\hat{\mathbf{x}}, \mathbf{x}) = \frac{1}{N} \sum_{i=1}^N \min_{m=1}^M \|\hat{\mathbf{x}}_{m,F}^i - \mathbf{x}_{m,F}^i\|_2^2$$

C. Experiments

We propose two main experiments to assess the performance of our framework. The first experiment studies the benefit of our proposed scene representation strategy. The second experiment explores the generalization of our model across airports. Below, describe each experiment in more detail.

1. Scene Representation Strategy

We hypothesize that our scene selection strategy, described Section IV.B, produces complex and interesting scene representations as it prioritizes more critical interactions and agent motion profiles within a scene. The objective of this experiment is, thus, to assess the proposed selection approach and our model’s performance under it. To do so, we compare against a baseline selection approach in which K agents are randomly chosen to represent a scene.

We perform this experiment on a *single-airport* setting, where *Amelia-TF* is trained and tested on one airport at a time. To analyze our scene representation method, we first show scene representation statistics in Table 4 for each airport sub-experiment. Then, to analyze the model’s predictions, we report mADE/mFDE values under the *random* and *critical* selection strategies in Table 5 both at $F = 20$ (short-term) and $F = 50$ (long-term) and show qualitative results at $F = 50$ in Figure 8.

2. Generalization across Airports

We hypothesize that as we cover a wider variety of training data, our model will learn richer representations that would generalize better to unseen airport layouts and interactions. This would eventually reduce the requirement for more training data and/or adaptation techniques, such as fine-tuning. Thus, we propose a *multi-airport* ablation to assess *Amelia-TF*’s performance in *unseen* airports as we vary the number of *seen* ones during training. Specifically, we run 6 experiments: 1-Seen, 2-Seen, 3-Seen, 4-Seen, 7-Seen, and All-Seen, each of which is named after the number of airports seen during training. Here, the experiments with a larger number of *seen* airports are supersets of the experiments with a smaller number. To select the order for the seen airports, we first rank the airports by the number of total unique data points reported in Table 2. Then, we add airports to the seen set, starting from the middle of the list.

For these experiments, we use the proposed scene representation strategy. For brevity, we show mADE/mFDE results at $F = 20$ in Table 6 but we include results at $F = 50$ in the Appendix V.C.2. For reference, we also compare and discuss the generalization experiments against the single-airport setting.

VI. Results

In this section, we provide a detailed analysis for each of the experiments in Section V.C.

A. Scene Representation Strategy

In Table 4, we first analyze the ego-selection statistics of our scene representation strategy. We, thus, first summarize the per-airport, and ego-agent selection statistics for both, the random strategy (left) and our proposed strategy (right). The summary comprises the total number of ego-agents, the percentage corresponding to stationary agents, and the average closest meter distance between the agent and the closest hold-line (a.k.a. conflict point). For the latter, we report distances for all ego-agents, as well as stationary and moving agents separately. For each column of the proposed strategy, we show in parentheses the average percentage change w.r.t. the random strategy. The summary shows, that our proposed strategy generally selects agents with more dynamic profiles as depicted by the **15%** average reduction for the percentage of selected stationary ego-agents. The table further shows that our strategy generally selects agents that are closer to conflict regions compared to the random strategy.

Table 4 Ego-agent selection statistics for the *random* and *critical* strategies under the *single-airport* setting. In parentheses, we show the relative percentage difference between relevant and random strategies.

Airport	Total Num. Ego-agents	Random Selection Strategy				Critical Selection Strategy			
		Stationary Ego-agents (%)	Avg. Closest Dist. to Conflict Point (m)			Stationary Ego-agents (%)	Avg. Closest Dist. to Conflict Point (m)		
			All Agents	Stationary Agents	Moving Agents		All Agents	Stationary Agents	Moving Agents
PANC	481,353	1.84	74.44	74.15	107.87	1.75 (-4.89%)	72.26 (-2.93%)	72.08 (-2.80%)	96.40 (-10.64%)
KBOS	435,162	15.28	82.30	69.43	153.66	11.30 (-26.05%)	70.44 (-14.42%)	60.44 (-12.95%)	148.96 (-3.06%)
KDCA	455,366	43.92	103.48	95.84	113.25	36.84 (-16.12%)	99.61 (-3.74%)	92.25 (-3.74%)	112.23 (-0.90%)
KEWR	195,615	10.58	95.14	92.95	113.62	7.97 (-24.67%)	83.29 (-12.45%)	81.40 (-12.43%)	105.12 (-7.49%)
KJFK	54,458	38.29	88.30	78.38	104.27	30.60 (-20.08%)	74.79 (-15.30%)	68.42 (-12.71%)	89.23 (-14.43%)
KLAX	125,602	5.26	50.55	49.24	74.04	4.27 (-18.82%)	47.01 (-6.99%)	46.52 (-5.53%)	58.15 (-21.47%)
KMDW	268,734	9.49	66.58	70.54	28.84	9.91 (4.43%)	58.14 (-12.69%)	61.93 (-12.21%)	23.69 (-17.86%)
KMSY	673,439	17.69	147.63	149.73	137.85	17.87 (1.02%)	144.20 (-2.32%)	146.11 (-2.42%)	135.41 (-1.77%)
KSEA	85,948	4.51	81.19	79.17	124.06	3.24 (-28.16%)	77.57 (-4.45%)	76.15 (-3.81%)	120.03 (-3.25%)
KSFO	186,436	26.22	82.76	78.19	95.62	20.70 (-21.05%)	68.25 (-17.54%)	65.34 (-16.44%)	79.42 (-16.95%)
Average	296,211	17.31	87.24	83.76	105.31	14.45 (-15.44%)	79.55 (-9.28%)	77.06 (-8.50%)	96.86 (-9.78%)

Note: The percentage of stationary agents and the average closest distance to a conflict point are reported for the test set.

Next, in Table 5 we compare our model’s performance for short- and long-term predictions (i.e., $F = 20$ s and $F = 50$ s). As before, we show the relative percentage change between the proposed strategy and the random strategy for the corresponding metric. Here green values (negative percentages) indicate an improvement upon the baseline while red values (positive percentages), a decrease. While we see a decrease in mADE/mFDE performance across most airports when our strategy is used, we believe this result is expected since our selection methodology is designed to prioritize agents with high interactive and dynamic motion profiles, making the task inherently more challenging. The latter is supported by the summary presented in Table 4.

Table 5 Model performance comparison between the *random* and *critical* scene representation strategies under the *single-airport* setting. We show mADE/mFDE values (in meters) at $F = 20$ and $F = 50$. The percentages shown in parentheses represent the relative difference between the two strategies.

Airport	Random Selection Strategy				Critical Selection Strategy			
	mADE@20 (m)	mFDE@20 (m)	mADE@50 (m)	mFDE@50 (m)	mADE@20 (m)	mFDE@20 (m)	mADE@50 (m)	mFDE@50 (m)
PANC	6.54	12.77	22.93	54.11	10.11 (+54.65%)	20.87 (+63.44%)	38.84 (+69.39%)	101.89 (+88.32%)
KBOS	5.12	10.02	19.28	48.05	5.58 (+9.04%)	10.90 (+8.85%)	21.34 (+10.67%)	53.76 (+11.88%)
KDCA	5.75	10.54	18.13	41.60	4.74 (-17.66%)	9.22 (-12.51%)	16.42 (-9.45%)	40.57 (-2.49%)
KEWR	6.50	12.78	22.69	54.17	6.61 (+1.69%)	12.92 (+1.08%)	23.68 (+4.35%)	57.63 (+6.38%)
KJFK	3.66	7.70	13.50	32.98	4.58 (+25.21%)	9.52 (+23.64%)	17.11 (+26.79%)	41.19 (+24.92%)
KLAX	11.38	20.29	38.28	92.14	11.36 (-0.14%)	20.63 (+1.67%)	36.08 (-5.73%)	88.25 (-4.22%)
KMDW	2.97	5.51	9.82	22.77	3.30 (+11.33%)	6.12 (+10.96%)	11.50 (+17.17%)	28.80 (+26.47%)
KMSY	2.43	4.53	8.53	21.25	2.73 (+12.39%)	5.12 (+12.84%)	9.89 (+16.00%)	25.68 (+20.83%)
KSEA	7.81	15.24	25.52	57.52	9.76 (+24.96%)	18.35 (+20.36%)	29.94 (+17.33%)	65.82 (+14.44%)
KSFO	5.09	9.69	16.45	37.61	5.06 (-0.49%)	9.82 (+1.39%)	17.05 (+3.64%)	40.23 (+6.97%)
Average	5.72	10.91	19.51	46.22	6.38 (+11.33%)	12.35 (+13.19%)	22.18 (+13.70%)	54.38 (+17.66%)

Nevertheless, we observe that the absolute difference between the mADE/mFDE of the two strategies is generally less than a few meters. We believe this showcases the strength of our model’s learning capabilities despite being trained on more challenging scenarios. Finally, we compare qualitative results for both strategies in Figure 8. We show 60s

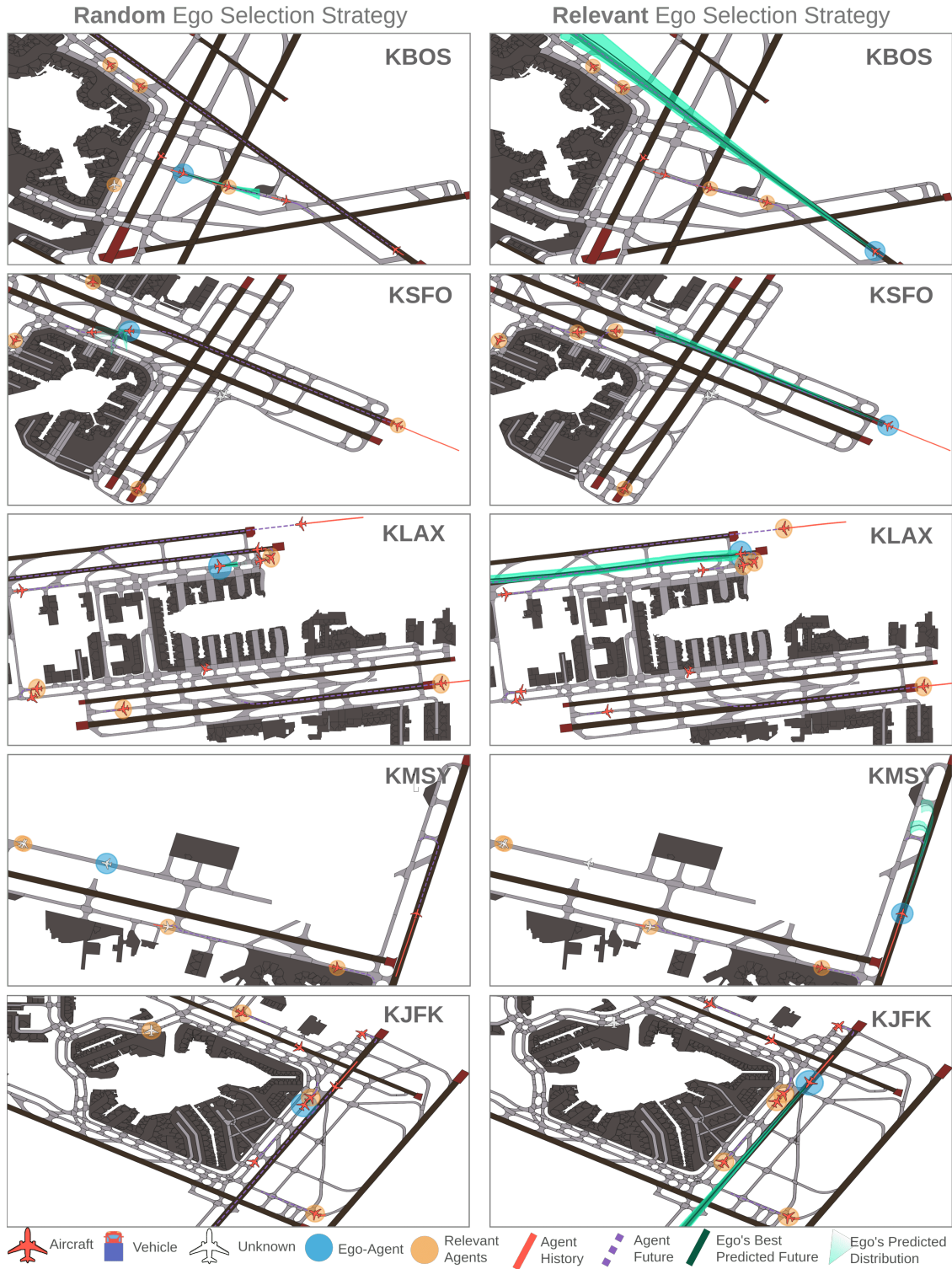


Fig. 8 Scene representation and prediction results for the *random* (left column) and *critical* (right column) scene representation strategies under the *single-airport* setting, showing that the proposed strategy generally selects agents with a more relevant kinematic and interactive profile. The shown prediction lengths are $F = 50$ s.

scenes where the 10 first seconds represent each agent’s history (solid red segment) and the subsequent 50s represent their future (dashed purple segment for ground truth and green segment for prediction). We show paired scenes for various airports depicting all agents in the scene, the K-relevant agents (orange halo), and the selected ego-agent (blue halo). Within this figure, we can see that our selection strategy often selects more dynamic agents, e.g., aircraft preparing for take-off or landing, as well as agents in conflicting regions, e.g., aircraft vacating a taxiway. Moreover, the agent-to-agent relationships between the selected relevant agents within our strategy are generally more critical. For example, our strategy often selects aircraft that are either vacating or potentially crossing through a runway that’s soon to be used by another aircraft preparing for take-off. In contrast, the random strategy more often selects less dynamic agents, as well as agents whose relationships may not be critical.

B. Generalization across Airports

Table 6 summarizes the results from our *multi-airport* experiment sweep described in Section V.C.2. Each column shows the mADE/mFDE results for a given airport’s test set and the last column shows the average mADE/mFDE across all airports. For reference, the first row on the table shows the *single-airport* results obtained under the *critical* scene selection strategy. Each of the remaining rows represents an experiment. The white and gray cells represent the *seen* and *unseen* airports for the given experiment, respectively. We highlight in **bolded text** the best mADE and mFDE values across the experiment sweep and in **green** the mADE and mFDE values that were lower than the results obtained through the *single-airport* setting. While there’s a minor cost in performance across the seen sets, our experiments show that, overall, the generalization across unseen airports improves significantly as we increase the variety and amount of training data. We show, for instance, that the 7-Seen experiment achieves the lowest average mADE/mFDE from the full sweep of experiments. Furthermore, its average results across all airports as well the results for KSEA, KDCA, PANC and KLAX as lower than those obtained through the *single-airport* setting.

Table 6 We show results for the *multi-airport* experiment for a prediction horizon of $F = 20$. In each row, we highlight in light gray the airports that were not included in the experiment’s training set, i.e., the *unseen* airports. In the final column, we show the average mADE/mFDE across all airports. Bolded values represent the lowest mADE and mFDE across the sweep. We highlight in green values that were lower than the *single-airport* experiment. All results are shown in meters.

Experiment	KMDW	KEWR	KBOS	KSFO	KSEA	KDCA	PANC	KLAX	KJFK	KMSY	Average
	mADE / mFDE	mADE / mFDE	mADE / mFDE	mADE / mFDE	mADE / mFDE	mADE / mFDE	mADE / mFDE	mADE / mFDE	mADE / mFDE	mADE / mFDE	mADE / mFDE
Single-Airport	3.30 / 6.12	6.61 / 12.92	5.58 / 10.90	5.06 / 9.82	9.76 / 18.35	4.74 / 9.22	10.11 / 20.87	11.36 / 20.63	4.58 / 9.52	2.73 / 5.12	6.38 / 12.35
1-Seen	3.30 / 6.12	13.76 / 30.91	11.30 / 25.58	9.68 / 21.73	14.07 / 31.44	7.80 / 16.07	15.00 / 33.75	15.49 / 33.13	7.40 / 16.77	7.43 / 17.11	10.52 / 23.26
2-Seen	3.31 / 6.23	6.92 / 13.45	8.17 / 17.63	7.49 / 17.18	10.57 / 22.86	6.04 / 12.47	10.61 / 23.00	12.78 / 26.34	5.21 / 11.15	4.49 / 9.64	7.56 / 15.99
3-Seen	3.26 / 6.59	7.25 / 14.20	6.05 / 12.11	7.25 / 15.50	9.90 / 20.95	6.16 / 12.74	9.53 / 20.26	10.99 / 21.86	4.96 / 10.54	4.33 / 9.29	6.97 / 14.40
4-Seen	3.52 / 6.74	7.26 / 14.33	6.31 / 12.68	5.66 / 11.33	9.79 / 20.42	5.99 / 12.28	9.22 / 19.14	10.70 / 21.16	4.80 / 10.27	4.18 / 9.05	6.74 / 13.74
7-Seen	3.59 / 7.03	7.30 / 14.54	6.59 / 13.59	5.73 / 11.65	8.30 / 16.71	4.55 / 8.82	7.48 / 14.94	9.99 / 19.35	4.66 / 9.96	4.64 / 9.85	6.28 / 12.64
All-Seen	3.88 / 7.70	7.87 / 15.80	6.87 / 14.34	6.09 / 12.64	9.03 / 18.35	4.84 / 9.55	8.24 / 16.75	8.80 / 16.73	4.56 / 9.64	3.22 / 6.25	6.34 / 12.77

Finally, we show qualitative examples for the generalization experiment in Figure 9. We leverage the 7-Seen experiment to showcase the performance of the model in *seen* airports (left column) vs. *unseen* ones (right column). In particular, the figure shows the model’s predictions on four common aircraft operations: take-off roll (first row), landing (second), vacating a runway upon landing (third), and taxiing in preparation for take-off (fourth). Through varying airport topologies and agent distributions within the map, these results show that Amelia-TF is able to make strong long-term predictions for each of the tasks in both settings.

VII. Discussion

This section provides conclusions and discusses future work and avenues for both the Amelia-48 dataset and the Amelia-TF model.

A. Conclusion

The two goals of this work are to introduce and open-source a large-scale dataset for airport surface movement, Amelia-48 and also introduce a large transformer-based trajectory forecasting model, Amelia-TF. As part of our large-scale Amelia-48, we also provide lightweight graph representations of the airport maps as well as our methodology for generating such representation. We validate our dataset and post-processing pipelines by providing statistical

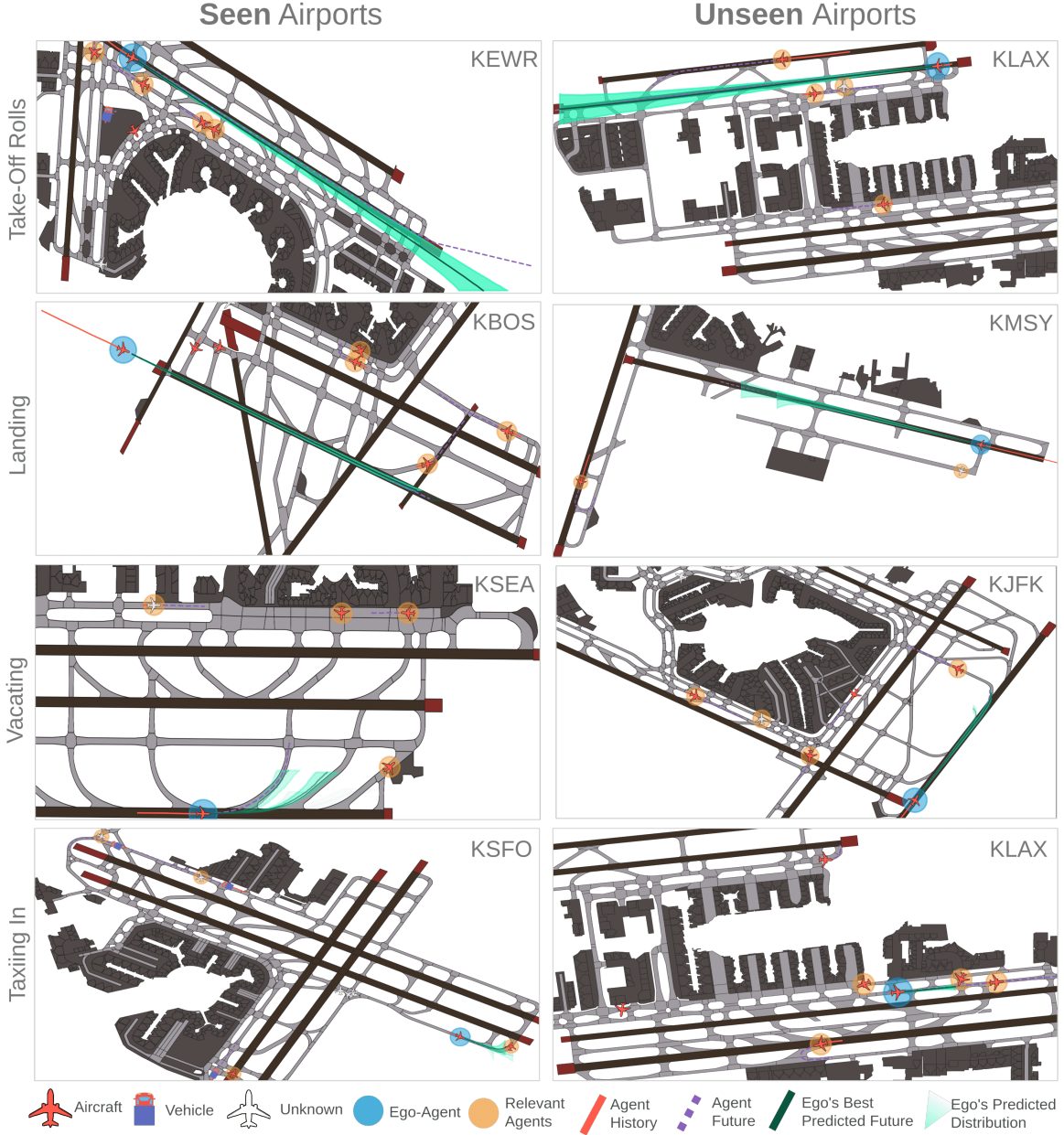


Fig. 9 Prediction results for the 7-Seen experiment on four different tasks: take-off roll, landing, vacating a runway, and taxiing. We show the strong generalization capabilities of our model by comparing results for *seen* (left column) and *unseen* airports (right column). The shown prediction lengths are $F = 50s$.

analyses, visualizations and insights for 10 major airports within the US. To the best of the authors' knowledge, this is the **largest dataset of its kind in the public domain** specifically geared toward training next-generation data-driven predictive models for airport surface operations.

This work also introduces *Amelia-TF*, a large transformer-based trajectory forecasting model trained on 9.4 billion tokens of the processed dataset. *Amelia-TF* focuses on encoding relevant scene representations via scene characterization methodologies [52], and designed to provide multi-future zero-shot generalization capabilities to previously unseen airports. The work provides details on the design choices and training recipes to enable replication of results and downstream use for various subtasks. The generalization qualities are investigated on held-out airports using rigorous performance analysis for short- and long-term prediction horizons. The results across our experiments

showcase the strong performance of *Amelia*-TF across various axes of analysis, exhibiting strong generalization to multiple airports in seen vs unseen settings. To date, this is the **first multi-airport generalizable airport surface trajectory forecasting model in the public domain** and we invite other researchers to use the strong multi-future modeling capabilities for various downstream tasks like collision risk assessment, anomaly detection, taxi-out time predictions, etc.

B. Limitations & Future Work

While our work represents a significant step forward in terms of scale and development of data-driven methodologies to study behavior and operations in airports, we believe that further developments are necessary to support future research in this field. Therefore, we outline potential future directions for this work.

1. Scaling the Dataset and Model

Within our experimental setup, our largest model thus far has been trained on 12 months of data from 10 different airports. While the latter comprises over **9.4B** tokens representing positional data from more than **19M** scenes, we believe further scaling and model improvements are needed to cover a larger, more diverse space of airport operations and improve long-term generalization performance. On the dataset end, we plan to continue collecting more SWIM SMES data. Phase 2 of data collection started on Dec 1st, 2023, and is expected to continue until Dec 1st, 2024. Further scaling, however, would also necessitate changes to the model that help improve the efficiency and performance of the model. In our work, we focused on representing scenes scoring and characterizing the kinematic and interactive profiles for each agent and selecting the most *relevant* ones. One promising direction, thus, is to further explore and study different scene representation and scene encoding strategies for capturing agent-to-agent and agent-to-map relationships more effectively.

2. Future Applications

Predictive models for airport operations can be used for various downstream tasks. A future direction would include showcasing the performance of the *Amelia*-TF model for such tasks. Data-driven collision risk assessments (CRA) can reduce the number of false alarms and help in mitigating near misses. The *Amelia*-TF model can be combined with provably safe methods like conformal predictions [9], confidence-based reachability analysis [55] and evidential neural networks [56]. To evaluate CRA methods, one avenue would be to mine the *Amelia*-48 dataset for reported incidents. Nominally, this can be achieved by manually querying the Aviation Safety Reporting System (ASRS) or Aviation Safety Information Analysis and Sharing System (ASIAS) and then locating the data. These examples can be used to train or evaluate safety-critical anomaly detection methods thereby improving the models and providing a consistent benchmarking in the aviation domain. *Amelia*-TF model can also be used downstream for improving taxi-out time predictions, departure metering and time-of-arrival calculations.

Acknowledgments

This work was supported by Boeing (award #2022UIPA422). This work used Bridges-2 at Pittsburgh Supercomputing Center through allocation c1s220039p from the Advanced Cyberinfrastructure Coordination Ecosystem: Services & Support (ACCESS) program, which is supported by National Science Foundation grants #2138259, #2138286, #2138307, #2137603, and #2138296. This work was also supported by the Korean Ministry of Trade, Industry, and Energy (MOTIE; grant #P0026022), and by the Korea Institute of Advancement of Technology (KIAT), through the International Cooperative R&D program (#P0019782): Embedded AI Based fully autonomous driving software and Maas technology development.

References

- [1] Daugherty, A., “‘We were very lucky’: Near-collisions spark new worries for air travel,” *POLITICO*, 2023.
- [2] Ember, S., and Steel, E., “Airline Close Calls Happen Far More Often Than Previously Known,” *The New York Times*, 2023.
- [3] Association, I. A. T., “Air Passenger Market Analysis - December 2022,” Tech. rep., IATA, 2022.
- [4] TSA, “Transportation Security Administration checkpoint travel numbers,” , 2023. URL <https://www.tsa.gov/travel/passenger-volumes>.

- [5] Aratani, L., “TSA broke record on Sunday for number of passengers screened,” *The Washington Post*, 2023.
- [6] Badrinath, S., Abel, J., Balakrishnan, H., Joback, E., and Reynolds, T., “Spatial Modeling of Airport Surface Fuel Burn for Environmental Impact Analyses,” *Journal of Air Transportation*, 2023, pp. 1–13.
- [7] Behere, A., and Mavris, D. N., “A Method for the Parametric Representation of Take-off Time-Series Trajectory Data for Environmental Impact Assessment,” *AIAA AVIATION 2023 Forum*, 2023, p. 4111.
- [8] Degas, A., Islam, M. R., Hurter, C., Barua, S., Rahman, H., Poudel, M., Ruscio, D., Ahmed, M. U., Begum, S., Rahman, M. A., et al., “A survey on artificial intelligence (ai) and explainable ai in air traffic management: Current trends and development with future research trajectory,” *Applied Sciences*, Vol. 12, No. 3, 2022, p. 1295.
- [9] Muthali, A., Shen, H., Deglurkar, S., Lim, M. H., Roelofs, R., Faust, A., and Tomlin, C., “Multi-agent reachability calibration with conformal prediction,” *arXiv preprint arXiv:2304.00432*, 2023.
- [10] Sui, D., Chen, H., and Zhou, T., “A Conflict Resolution Strategy at a Taxiway Intersection by Combining a Monte Carlo Tree Search with Prior Knowledge,” *Aerospace*, Vol. 10, No. 11, 2023, p. 914.
- [11] Kong, Y., and Mahadevan, S., “Identifying Anomalous Behavior in Aircraft Landing Trajectory Using a Bayesian Autoencoder,” *Journal of Aerospace Information Systems*, 2023, pp. 1–9.
- [12] Memarzadeh, M., Matthews, B. L., and Weckler, D. I., “Anomaly Detection in Flight Operational Data Using Deep Learning,” *System-Wide Safety Technical Challenge 1 Close Out Event*, 2023.
- [13] Ranson, L., “FAA completes roll-out of ASDE-X anti-incursion surveillance,” *Flight International*, Vol. 180, No. 5313, 2011, pp. 15–15.
- [14] Zhang, X., Zhong, S., and Mahadevan, S., “Airport surface movement prediction and safety assessment with spatial–temporal graph convolutional neural network,” *Transportation research part C: emerging technologies*, Vol. 144, 2022, p. 103873.
- [15] Park, D. K., and Kim, J. K., “Influential factors to aircraft taxi time in airport,” *Journal of Air Transport Management*, Vol. 106, 2023, p. 102321.
- [16] Navarro, I., Patrikar, J., Dantas, J. P. A., Baijal, R., Higgins, I., Scherer, S., and Oh, J., “SoRTS: Learned Tree Search for Long Horizon Social Robot Navigation,” *IEEE Robotics and Automation Letters*, Vol. 9, No. 4, 2024, pp. 3759–3766. <https://doi.org/10.1109/LRA.2024.3370051>.
- [17] Patrikar, J., Dantas, J., Ghosh, S., Kapoor, P., Higgins, I., Aloor, J. J., Navarro, I., Sun, J., Stoler, B., Hamidi, M., et al., “Challenges in close-proximity safe and seamless operation of manned and unmanned aircraft in shared airspace,” *arXiv preprint arXiv:2211.06932*, 2022.
- [18] Liu, Y., Hansen, M., Gupta, G., Malik, W., and Jung, Y., “Predictability impacts of airport surface automation,” *Transportation Research Part C: Emerging Technologies*, Vol. 44, 2014, pp. 128–145.
- [19] Lee, H., Malik, W., and Jung, Y. C., “Taxi-out time prediction for departures at Charlotte airport using machine learning techniques,” *16th AIAA Aviation Technology, Integration, and Operations Conference*, 2016, p. 3910.
- [20] Wang, F., Bi, J., Xie, D., and Zhao, X., “A data-driven prediction model for aircraft taxi time by considering time series about gate and real-time factors,” *Transportmetrica A: Transport Science*, Vol. 19, No. 3, 2023, p. 2071353.
- [21] Alsalous, O., and Hotle, S., “Deicing Facility Capacity and Delay Estimation Using ASDE-X Data: Chicago O’Hare Simulation Case Study,” *Transportation Research Record*, 2023, p. 03611981231185147.
- [22] Gui, X., Zhang, J., Peng, Z., and Yang, C., “Data-driven method for the prediction of estimated time of arrival,” *Transportation Research Record*, Vol. 2675, No. 12, 2021, pp. 1291–1305.
- [23] Vaswani, A., Shazeer, N., Parmar, N., Uszkoreit, J., Jones, L., Gomez, A. N., Kaiser, Ł., and Polosukhin, I., “Attention is all you need,” *Advances in neural information processing systems*, Vol. 30, 2017.
- [24] Lerner, A., Chrysanthou, Y., and Lischinski, D., “Crowds by Example,” *Comput. Graph. Forum*, Vol. 26, No. 3, 2007, pp. 655–664. <https://doi.org/10.1111/j.1467-8659.2007.01089.x>, URL <https://doi.org/10.1111/j.1467-8659.2007.01089.x>.
- [25] Pellegrini, S., Ess, A., Schindler, K., and Gool, L. V., “You’ll never walk alone: Modeling social behavior for multi-target tracking,” *IEEE 12th International Conference on Computer Vision, ICCV 2009, Kyoto, Japan, September 27 - October 4, 2009*, IEEE Computer Society, 2009, pp. 261–268. <https://doi.org/10.1109/ICCV.2009.5459260>, URL <https://doi.org/10.1109/ICCV.2009.5459260>.

- [26] Robicquet, A., Alahi, A., Sadeghian, A., Anenberg, B., Doherty, J., Wu, E., and Savarese, S., “Forecasting Social Navigation in Crowded Complex Scenes,” *CoRR*, Vol. abs/1601.00998, 2016.
- [27] Rudenko, A., Palmieri, L., Herman, M., Kitani, K. M., Gavrila, D. M., and Arras, K. O., “Human motion trajectory prediction: a survey,” *Int. J. Robotics Res.*, Vol. 39, No. 8, 2020. <https://doi.org/10.1177/0278364920917446>, URL <https://doi.org/10.1177/0278364920917446>.
- [28] Sun, P., Kretzschmar, H., Dotiwalla, X., Chouard, A., Patnaik, V., Tsui, P., Guo, J., Zhou, Y., Chai, Y., Caine, B., et al., “Scalability in perception for autonomous driving: Waymo open dataset,” *Proceedings of the IEEE/CVF conference on computer vision and pattern recognition*, 2020, pp. 2446–2454.
- [29] Chang, M., Lambert, J., Sangkloy, P., Singh, J., Bak, S., Hartnett, A., Wang, D., Carr, P., Lucey, S., Ramanan, D., and Hays, J., “Argoverse: 3D Tracking and Forecasting With Rich Maps,” *IEEE Conference on Computer Vision and Pattern Recognition, CVPR 2019, Long Beach, CA, USA, June 16-20, 2019*, Computer Vision Foundation / IEEE, 2019, pp. 8748–8757. <https://doi.org/10.1109/CVPR.2019.00895>, URL http://openaccess.thecvf.com/content_CVPR_2019/html/Chang_Argoverse_3D_Tracking_and_Forecasting_With_Rich_Maps_CVPR_2019_paper.html.
- [30] Caesar, H., Bankiti, V., Lang, A. H., Vora, S., Liong, V. E., Xu, Q., Krishnan, A., Pan, Y., Baldan, G., and Beijbom, O., “nuscnets: A multimodal dataset for autonomous driving,” *Proceedings of the IEEE/CVF conference on computer vision and pattern recognition*, 2020, pp. 11621–11631.
- [31] Li, M. Z., and Ryerson, M. S., “Reviewing the DATAS of aviation research data: Diversity, availability, tractability, applicability, and sources,” *Journal of Air Transport Management*, Vol. 75, 2019, pp. 111–130.
- [32] Patrikar, J., Moon, B., Oh, J., and Scherer, S., “Predicting like a pilot: Dataset and method to predict socially-aware aircraft trajectories in non-towered terminal airspace,” *2022 International Conference on Robotics and Automation (ICRA)*, IEEE, 2022, pp. 2525–2531.
- [33] Patrikar, J., Dantas, J., Moon, B., Hamidi, M., Ghosh, S., Keetha, N., Higgins, I., Chandak, A., Yoneyama, T., and Scherer, S., “TartanAviation: Image, Speech, and ADS-B Trajectory Datasets for Terminal Airspace Operations,” *arXiv preprint arXiv:2403.03372*, 2024.
- [34] Navarro, I., and Oh, J., “Social-PatteRNN: Socially-Aware Trajectory Prediction Guided by Motion Patterns,” *2022 IEEE/RSJ International Conference on Intelligent Robots and Systems (IROS)*, IEEE, 2022, pp. 9859–9864.
- [35] Ngiam, J., Vasudevan, V., Caine, B., Zhang, Z., Chiang, H.-T. L., Ling, J., Roelofs, R., Bewley, A., Liu, C., Venugopal, A., et al., “Scene transformer: A unified architecture for predicting future trajectories of multiple agents,” *International Conference on Learning Representations*, 2021, pp. 541–556.
- [36] Cui, A., Casas, S., Wong, K., Suo, S., and Urtasun, R., “Gorela: Go relative for viewpoint-invariant motion forecasting,” *2023 IEEE International Conference on Robotics and Automation (ICRA)*, IEEE, 2023, pp. 7801–7807.
- [37] Casas, S., Luo, W., and Urtasun, R., “Intentnet: Learning to predict intention from raw sensor data,” *Conference on Robot Learning*, PMLR, 2018, pp. 947–956.
- [38] Liang, M., Yang, B., Hu, R., Chen, Y., Liao, R., Feng, S., and Urtasun, R., “Learning lane graph representations for motion forecasting,” *Computer Vision—ECCV 2020: 16th European Conference, Glasgow, UK, August 23–28, 2020, Proceedings, Part II 16*, Springer, 2020, pp. 541–556.
- [39] Gao, J., Sun, C., Zhao, H., Shen, Y., Anguelov, D., Li, C., and Schmid, C., “Vectornet: Encoding hd maps and agent dynamics from vectorized representation,” *Proceedings of the IEEE/CVF Conference on Computer Vision and Pattern Recognition*, 2020, pp. 11525–11533.
- [40] Shi, S., Jiang, L., Dai, D., and Schiele, B., “Motion transformer with global intention localization and local movement refinement,” *Advances in Neural Information Processing Systems*, Vol. 35, 2022, pp. 6531–6543.
- [41] Kuo, Y.-L., Huang, X., Barbu, A., McGill, S. G., Katz, B., Leonard, J. J., and Rosman, G., “Trajectory prediction with linguistic representations,” *2022 International Conference on Robotics and Automation (ICRA)*, IEEE, 2022, pp. 2868–2875.
- [42] Nayakanti, N., Al-Rfou, R., Zhou, A., Goel, K., Refaat, K. S., and Sapp, B., “Wayformer: Motion forecasting via simple & efficient attention networks,” *2023 IEEE International Conference on Robotics and Automation (ICRA)*, IEEE, 2023, pp. 2980–2987.

- [43] Alahi, A., Goel, K., Ramanathan, V., Robicquet, A., Fei-Fei, L., and Savarese, S., “Social lstm: Human trajectory prediction in crowded spaces,” *Proceedings of the IEEE conference on computer vision and pattern recognition*, 2016, pp. 961–971.
- [44] Zhao, D., and Oh, J., “Noticing motion patterns: A temporal cnn with a novel convolution operator for human trajectory prediction,” *IEEE Robotics and Automation Letters*, Vol. 6, No. 2, 2020, pp. 628–634.
- [45] Yuan, Y., Weng, X., Ou, Y., and Kitani, K. M., “Agentformer: Agent-aware transformers for socio-temporal multi-agent forecasting,” *Proceedings of the IEEE/CVF International Conference on Computer Vision*, 2021, pp. 9813–9823.
- [46] Chai, Y., Sapp, B., Bansal, M., and Anguelov, D., “Multipath: Multiple probabilistic anchor trajectory hypotheses for behavior prediction,” *arXiv preprint arXiv:1910.05449*, 2019.
- [47] Yin, Y., Zhang, S., Zhang, Y., Zhang, Y., and Xiang, S., “Context-aware Aircraft Trajectory Prediction with Diffusion Models,” *2023 IEEE 26th International Conference on Intelligent Transportation Systems (ITSC)*, IEEE, 2023, pp. 5312–5317.
- [48] Robb, J., “System wide information management (SWIM): program overview and status update,” *2014 Integrated Communications, Navigation and Surveillance Conference (ICNS) Conference Proceedings*, IEEE, 2014, pp. 1–15.
- [49] Vinoski, S., “Advanced message queuing protocol,” *IEEE Internet Computing*, Vol. 10, No. 6, 2006, pp. 87–89.
- [50] Map, O. S., “Open street map,” *Online: <https://www.openstreetmap.org>. Search in*, 2014.
- [51] Boeing, G., “OSMnx: New methods for acquiring, constructing, analyzing, and visualizing complex street networks,” *Computers, Environment and Urban Systems*, Vol. 65, 2017, pp. 126–139.
- [52] Stoler, B., Navarro, I., Jana, M., Hwang, S., Francis, J., and Oh, J., “SafeShift: Safety-Informed Distribution Shifts for Robust Trajectory Prediction in Autonomous Driving,” *2024 IEEE Intelligent Vehicles Symposium (IV)*, 2024, pp. 1179–1186. <https://doi.org/10.1109/IV55156.2024.10588828>.
- [53] Melnychuk, V., Frauen, D., and Feuerriegel, S., “Causal transformer for estimating counterfactual outcomes,” *International Conference on Machine Learning*, PMLR, 2022, pp. 15293–15329.
- [54] Ho, J., Kalchbrenner, N., Weissenborn, D., and Salimans, T., “Axial attention in multidimensional transformers,” *arXiv preprint arXiv:1912.12180*, 2019.
- [55] Nakamura, K., and Bansal, S., “Online update of safety assurances using confidence-based predictions,” *2023 IEEE International Conference on Robotics and Automation (ICRA)*, IEEE, 2023, pp. 12765–12771.
- [56] Amini, A., Schwarting, W., Soleimany, A., and Rus, D., “Deep evidential regression,” *Advances in Neural Information Processing Systems*, Vol. 33, 2020, pp. 14927–14937.

Appendix

A. Architecture Details

Table 7 Architecture of *Amelia-TF*, inspired by [35, 39]. Here $T = 60, K = 5, D_x = 4, D_c = 7, D_e = 256, D_f = 7$.

Module	Input(s)	Output	Layer Type	Operation Description	Output Dimensions	Num. Parameters
Agent Feature Extractor ϕ^x	\mathbf{x}	a_1	Linear	–	$K \times T \times D_x$	1.3K
	a_1	a_2	LayerNorm	–	$K \times T \times D_e$	512
	a_2	a_3	ReLU	–	$K \times T \times D_e$	–
	a_3	$\bar{\mathbf{x}}$	Linear	–	$K \times T \times D_e$	65.8K
	$\bar{\mathbf{x}} + \text{PE}$	$\bar{\mathbf{x}}_{\text{PE}}$	Embedding	Time embedding	$K \times T \times D_e$	15.4K
Context Feature Extractor ϕ^c	\mathbf{c}	c_1	Linear	–	$K \times P \times D_c$	1.5K
	c_1	c_2	BatchNorm	–	$K \times P \times D_e$	200
	c_2	c_3	ReLU	–	$K \times P \times D_e$	–
	c_3	c_4	Linear	–	$K \times P \times D_e$	65.8K
	c_4	c_5	BatchNorm	–	$K \times P \times D_e$	200
	c_5	c_6	ReLU	–	$K \times P \times D_e$	–
	c_6	c_7	Linear	–	$K \times P \times D_e$	81.9K
	c_7	c_8	BatchNorm	–	$K \times P \times D_e$	6.4K
	c_8	c_9	ReLU	–	$K \times P \times D_e$	–
Scene Encoder	$\bar{\mathbf{x}}_{\text{PE}}$	e_1	Transformer	Self-attention across T	$K \times T \times D_e$	789K
	e_1	e_2	Transformer	Self-attention across K	$K \times T \times D_e$	789K
	$e_2, \bar{\mathbf{c}}$	e_3	Transformer	Cross-attention	$K \times T \times D_e$	789K
	e_3	e_4	Transformer	Self-attention across T	$K \times T \times D_e$	789K
	e_4	e_5	Transformer	Self-attention across K	$K \times T \times D_e$	789K
	$e_5, \bar{\mathbf{c}}$	e_6	Transformer	Cross-attention	$K \times T \times D_e$	789K
	e_6	e_7	Transformer	Self-attention across T	$K \times T \times D_e$	789K
	e_7	e_8	Transformer	Self-attention across K	$K \times T \times D_e$	789K
	e_8	e_9	Linear	Refinement Layer	$K \times T \times D_e$	525K
Scene Decoder	e_9	d_1	Linear	–	$M \times K \times T \times D_e$	16.6K
	d_1	d_2	GeLU	–	$M \times K \times T \times D_e$	–
	d_2	μ_x, Σ_x, ρ	Linear	–	$M \times K \times T \times D_f$	1.8K
	ρ	ρ	Softmax	Softmax across M	$M \times K \times T \times 1$	–

B. Training Details

Below we provide a complete list of our training hyperparameters:

- 1) **Framework:** Pytorch lightning (version 2.0.0), torch (version 2.0.0)
- 2) **Optimization:** AdamW (learning rate= 0.0001, weight decay= 0.1, $\beta_1 = 0.9, \beta_2 = 0.95$).
- 3) **Scheduler:** ReduceLROnPlateau (Monitors validation loss, patience= 10, factor= 0.1)
- 4) **Early Stopping:** Monitors mADE at $T = 50$, patience= 10.
- 5) **Other hyperparameters:** Max. epochs= 100, batch size= 128.
- 6) **Dataset:** Day-based splitting strategy (80% for training/validation, 20% for testing). One month of collected data per airport.
- 7) **Scene Representation:**
 - **Trajectories:** Scene length $T = 60$ ($H = 10, F = [20, 50]$), min. agents= 2, max. agents= 15, max. critical/relevant agents= 5, scene skip window= 1.
 - **Context:** Number of nodes per local context $P = 100$.
- 8) **Seed:** 42.

C. Supplementary Results

1. Long-term Generalization across Airports

Table 8 We show results for the *multi-airport* experiment for a prediction horizon of $F = 50$. In each row, we highlight in light gray the airports that were not included in the experiment’s training set, i.e., the unseen airports. In the final column, we show the average mADE/mFDE across all airports. All results are shown in meters.

Experiment	KMDW	KEWR	KBOS	KSFO	KSEA	KDCA	PANC	KLAX	KJFK	KMSY	Average
	mADE / mFDE	mADE / mFDE	mADE / mFDE	mADE / mFDE	mADE / mFDE	mADE / mFDE	mADE / mFDE	mADE / mFDE	mADE / mFDE	mADE / mFDE	mADE / mFDE
Single-Airport	11.50 / 28.80	23.68 / 57.63	21.34 / 53.76	17.05 / 40.23	29.94 / 65.82	16.42 / 40.57	38.84 / 101.89	36.08 / 88.25	17.11 / 41.19	9.89 / 25.68	22.18 / 54.39
1-Seen	11.50 / 28.80	56.14 / 140.59	48.16 / 124.34	40.54 / 103.97	54.24 / 130.67	28.90 / 73.87	61.62 / 156.56	63.20 / 164.52	29.51 / 73.97	30.59 / 80.23	42.44 / 107.75
2-Seen	11.84 / 29.89	24.62 / 59.04	34.89 / 88.52	31.69 / 78.28	40.37 / 96.33	24.00 / 62.72	43.30 / 107.04	48.91 / 122.31	20.54 / 51.20	19.29 / 51.33	29.94 / 74.67
3-Seen	12.46 / 31.81	25.15 / 57.29	23.20 / 56.48	28.33 / 67.40	35.70 / 81.02	24.32 / 59.55	38.85 / 92.94	39.02 / 91.96	19.37 / 47.06	19.53 / 51.52	26.59 / 63.70
4-Seen	12.71 / 31.64	25.54 / 59.18	23.88 / 58.45	19.78 / 46.72	33.36 / 73.86	22.40 / 54.04	35.24 / 83.90	36.42 / 85.11	18.58 / 43.97	17.93 / 47.47	24.58 / 58.43
7-Seen	14.35 / 38.62	26.83 / 66.12	27.57 / 71.84	20.81 / 50.01	28.29 / 64.69	16.40 / 41.25	27.40 / 66.74	34.60 / 85.90	17.71 / 42.84	19.87 / 54.56	23.38 / 58.26
All-Seen	15.30 / 40.91	28.76 / 70.23	28.52 / 73.57	22.63 / 53.78	30.41 / 68.98	17.86 / 44.88	30.19 / 72.78	29.73 / 72.46	17.00 / 40.92	12.31 / 33.04	23.27 / 57.16